



Nanopore Technology for Biomedical Applications

Tejal A. Desai,¹ Derek J. Hansford,² Lawrence Kulinsky,³ Amir H. Nashat,⁴ Guido Rasi,⁵ Jay Tu,⁶ Yuchun Wang,⁷ Miqin Zhang,⁸ and Mauro Ferrari⁹

Biomedical Microdevices Center, Bioengineering Graduate Group, Department of Materials Science and Mineral Engineering, Department of Civil and Environmental Engineering, University of California, Berkeley CA 94720

¹*Currently Assistant Professor, Department of Bioengineering, University of Illinois, Chicago IL 60607-7052*

²*Currently Assistant Professor, Biomedical Engineering Center, Department of Materials Science and Engineering, The Ohio State University, Columbus OH 43210*

³*Currently Research Scientist, Department of Materials Science and Mineral Engineering, University of California, Berkeley, 94720*

⁴*Currently Graduate Student, Department of Chemical Engineering, Massachusetts Institute of Technology, Cambridge MA 02139*

⁵*Istituto di Medicina Sperimentale, Consiglio Nazionale Ricerche, Rome, Italy*

⁶*Senior Engineer, Alien Technology, Hayward, CA 94545*

⁷*Currently Process Engineer, Chemical Mechanical Polishing Division, Applied Materials, Inc. Santa Clara, CA 95054*

⁸*Currently Assistant Professor, Department of Materials Science and Engineering, University of Washington, Seattle, WA 98195*

⁹*Director of the Center. Currently Professor of Internal Medicine, Professor of Mechanical Engineering, and Director, Biomedical Engineering Center, The Ohio State University, Columbus OH 43210*

Abstract. The ability to create well-defined and controlled interfaces has been an area of great interest over the last few years, particularly in the biomedical arena. This paper will describe the development of technology for the fabrication of nanopore membranes, and their operation in biological environments. With monodisperse pores sizes as small as 10 nanometers, these membranes offer advantages in their reproducibility, and their ability to be integrated with controlled biochemical surface modification protocols. A comprehensive review of results in the areas of nanopore and biocapsule microfabrication technologies, biocompatibility of nanomembrane materials, biologically appropriate post-processing protocols (bonding, sterilization), surface modification protocols, and appropriate mass transport models will be presented. The results point to the potential of using such technologies for therapeutic applications including immunoisolation biocapsules, drug delivery devices, and targeted biorecognition platforms.

Key Words. BioMEMS, nanotechnology, microfabrication, membranes, silicon

1. Introduction

Research on microfabricated devices for biomedical applications (BioMEMS) has rapidly advanced in the last few years. The suitability of such devices has been widely documented with extensive research and

development efforts in universities as well as private laboratories and companies. Several specialized congresses and symposia are periodically organized and dedicated to this field by professional societies such as the SPIE, IEEE, and ASME, and commercial entities such as the Cambridge HealthTech Institute, International Business Communication, and The Knowledge Foundation. Since 1998, the research and development communities in the field are served by the international archival journal “Biomedical Microdevices: BioMEMS and Biomedical Nanotechnology”.

The establishment and rapid growth of the field has been largely fueled by research primarily focused on the development of diagnostic tools such as combinatorial biochemistry on-a-chip (Fodor, 1997) electrophoretic and DNA analysis (Wooley and Mathies, 1994; Huang et al., 1992; Effenhauser et al., 1995; Harrison et al., 1993), chromatographic, biosensor, and cell manipulation and analysis systems (Baxter et al., 1994; McConnell et al., 1992; Volkmuth et al., 1995; Gourley, 1996), with relatively few researchers have concentrated on therapeutics. Some of the recent therapeutic applications of microfabrication technology include neural regeneration (Akin et al., 1994; Kovacs and Storment, 1994), CNS

stimulation (Wise, 1990; Edell et al., 1982), and pulsatile drug-delivery (Santini, et al., 1999).

We have concentrated our research efforts on the development of technology for the fabrication of nanopore membranes, and their operation in biological environments. With monodisperse pores sizes as small as 10 nanometers, these membranes offer additional competitive advantages in their reproducibility, and their ability to be integrated with controlled biochemical surface modification protocols, and as the 'ground floor' for further incorporation of micro electromechanical elements. It is noted that the protocols employed in the fabrication of the membranes are standard in MEMS processing—thus we retain the prefix "micro" as in "microfabricated nanomembranes", with no dimensional contradiction, for 'nano' is a dimensional indicator, while 'micro' in this context refers to conventional lithography-based manufacturing routes.

In view of the properties of the nanomembranes and biocapsules, our research has been guided by applications in the domains of bioseparation, and the delivery of therapeutic biomolecules from immunoisolated cell transplants and passive reservoirs. The full fruition of these technologies relies on the attainment of milestones in multiple domains:

- The reliable establishment of nanopore and biocapsule microfabrication technologies,
- The verification of benign cell and tissue interaction properties for the nanomembrane material and the biocapsule technology of choice,
- The establishment of biologically appropriate post-processing protocols (bonding, sterilization)
- The development of successful surface biomodification protocols for hemocompatibility, protein resistance, and immunografting, and
- The establishment and corroboration of mass transport models.

In this paper, we present the first comprehensive review of the results of our research in each of these areas.

2. Micromanufacturing of Nanomembranes and Biocapsules

2.1. Background on immunoisolation biocapsules

The concept of a biocapsule emerged over thirty years ago, as a possible way in which transplanted tissue could be protected from immune rejection by enclosure within a semipermeable membrane (Lim and Sun, 1980). Ideally, in diabetic patients, transplantation of pancreatic islet cells (allografts or xenografts) could restore normoglycemia. However, as with most tissue or cellular

transplants, the islet grafts, particularly xenografts, are subjected to immunorejection in the absence of chronic immunosuppression. To overcome this need for immunosuppressive drugs, the concept of isolating the islets from the recipient's immune system within biocompatible semipermeable capsules was developed (Colton and Avgoustiniatos, 1991; Scharp et al., 1984; Lanza et al., 1992). In principle, the biocapsules allow for the free diffusion of glucose, insulin, and other essential nutrients for the islets, while inhibiting the passage of larger entities such as antibodies and complement components (O'Shea et al., 1984). This selective permeability can allow for the physiological functioning of the islets, while preventing acute and chronic immunorejection.

The requirements for an immunoisolating biocapsule are numerous. In addition to well-controlled pore size, the capsule must exhibit stability, non-biodegradability, and biocompatibility. Most encapsulation methods to date have used polymeric semipermeable membranes (Goosen et al., 1985; Lafferty, 1989; Weber et al., 1991; Calafiore et al., 1990; Sugamori, 1989; Gerasimidi-Vazeo et al., 1992). However, these membranes have exhibited insufficient resistance to organic solvents, inadequate mechanical strength, and broad pore size distributions—all of which eventually lead to destruction of cell xenografts (Altman et al., 1991; Lacy et al., 1992). The most common method of immunoisolation, that of polymeric microcapsules, have the disadvantage of limited retrievability and possible mechanical failure of the spherical membrane. These characteristics may limit the use of microcapsules for non-immunosuppressed xenotransplantation (Ross, 1993; Colton, 1995). Although the area of biohybrid artificial organs has been researched extensively over the past few decades, certain technical problems may limit the clinical application of implantable immunoisolation devices. These problems are usually associated with device design and performance, particularly transport requirements. Due to these technical problems, the clinical success of encapsulated islet transplantation is still only minimal, with less than 30 documented cases of insulin independence occurring from over 250 attempts at clinical islet allo-transplantation since 1983 (Lanza and Chick, 1995).

By virtue of their biochemical inertness and relative mechanical strength, silicon and its oxides offer an alternative to the more conventional organic biocapsules. Contemporary advances in processing now permit the fabrication of sub-millimeter silicon-based devices with features in the tens of nanometer range (Ferrari et al., 1996). These capsules can provide the advantages of mechanical stability, uniform pore size distribution, and chemical inertness. By taking advantage of silicon bulk and surface material properties, structures can be

engineered to perform specific functions. Microfabrication technology may be advantageous in the field of tissue engineering by creating precisely controlled microenvironments to stimulate and enhance transplanted cell behavior. This promising technology brings together synthetic and non-synthetic components in order to replace lost or damaged tissue in a host. It has been widely shown that isolated cultured cells grow and organize in contact with synthetic materials that serve as scaffolds for the cells (Brendel et al. 1994). Therefore, silicon microfabrication of three-dimensional microenvironments for cells opens up many new possibilities in terms of tissue engineering and cell transplantation.

A further, and perhaps more important, advantage of microfabrication technology is the ability to fabricate membranes of specific pore size, allowing one to optimize the biocapsules specifically for the encapsulation of pancreatic islets. Current polymeric biocapsules have not been able to achieve uniform pore size membranes in the tens of nanometer range. By contrast, we have developed several variants of microfabricated diffusion barriers, containing pores with uniform dimensions as small as 20 nanometers (Chu and Ferrari, 1995). Furthermore, improved dynamic response of islets tissue can be obtained due to the reduced membrane thickness (9 μm) of microfabricated membranes compared to polymeric membranes (100–200 μm). It is important to retain rapid intrinsic secretion kinetics, in particular first phase insulin release (Colton and Avgoustiniatos, 1991), so as to provide physiological feedback control of blood glucose concentrations.

Using standard silicon integrated circuit and MEMS fabrication techniques such as photolithography, thin film deposition, and selective etching, membranes and biocapsules with nano- and micron- sized pores have been fabricated on a silicon wafer. Filters with highly uniform pores (<5% variation) between 0.01–10 μm in size have been fabricated in both encapsulated channel and membrane embodiments, as described below. The nominal pore size for the membrane filters is determined either by photolithography or the deposition and selective removal of a sacrificial layer (Chu and Ferrari, 1995), whereas for the encapsulated channel filters, controlled etching is used (Tu et al., 1998). Of particular interest to us are the specific separation of viruses during the blood fractionation process, and the blocking of antibodies and complement molecules from encapsulated xenogeneic cells. Of the three pore formation methods listed above, only controlled sacrificial layer deposition is precise enough to guarantee high pore uniformity at nanoscale dimensions. Using a thermally grown silicon dioxide (SiO_2) layer, we can presently control the thickness to $\pm 1 \text{ nm}$

for absolute pore sizes as small as 18 nanometers. With the recent advances in the semiconductor industry, this variation can be reduced to $\pm 1 \text{ \AA}$ for thicknesses as small as 50 \AA . With this protocol, we have successfully fabricated both membrane filters (Chu and Ferrari, 1995) and encapsulated-channel (Tu et al., 1998) (described in detail next).

2.2. Fabrication of membrane nanofilters

The microfabricated membrane is achieved through the use of bulk and surface micromachining. All designs of the microfabricated biocapsule consist of a surface-micromachined membrane on top of an anisotropically etched silicon wafer, which provides mechanical support (Brendel et al. 1994; Chu et al., 1996). Photolithography, in general, is not amenable to the fabrication of pores with dimensions smaller than 0.35–1.0 micrometer. To reach a desired pore size in the tens of nanometers range, we have developed strategies based on the use of a sacrificial oxide layer, sandwiched between two structural layers, for the definition of the pore pathways (Figure 1) (Chu and Ferrari, 1995). This strategy encompasses a multitude of viable embodiments for the biocapsules. The biocapsule membrane used for our *in vitro* studies can be fabricated using several different protocols, which allow membranes to be optimized. The specific configuration of the membrane pores, including pore size, density, and path length, can be fabricated as desired.

The pore channel is formed by sandwiching a SiO_2 sacrificial layer, the thickness of which determines the nominal pore size, between a polysilicon structural layer and the silicon wafer (Figure 2). For this design, increasing the number of entry holes maximizes the flux. PBS fluxes as high as 1.0 ml/cm²-hr have been attained for membrane filters with 30 nm-sized pores. Filtration tests showed 99% of 100 nanometer beads were retained with 50 nanometer pores. Although these can be operated as a flow-through filter with the filtrate entering from the top of the wafer, due to the reduced mechanical stability inherent in membrane systems, this

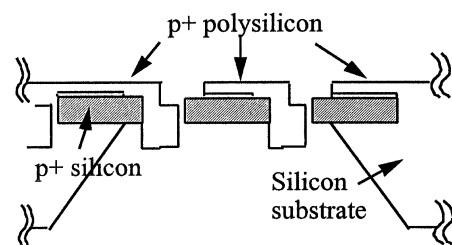


Fig. 1. Cross sectional view of membrane filter. The channel is formed between the p⁺ polys and p⁺ Si layer.

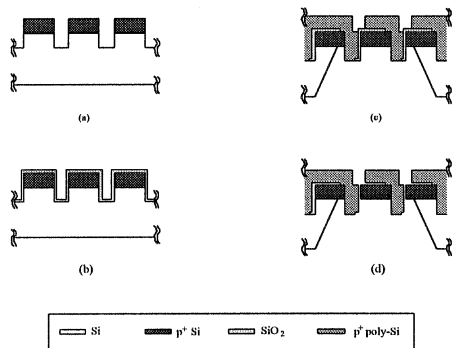


Fig. 2. Membrane process flow diagram.

filter can be put to better use as a diffusion barrier (Desai et al., 1999). By turning the structure upside-down, the filter may be employed as a well bounded by a membrane. Joining two of the membranes together produces a biocapsule.

The fabrication of the membrane filter uses a surface micromachining process, in which deposited polysilicon serves as a structural layer (Chu and Ferrari, 1995). In the first process step (Figure 2a), the top 6 μm of the silicon wafer is degenerately doped with boron to create a mechanically strong bottom structural layer. This layer will also serve as an etch-stop when the backside etch (Figure 2c) is performed. Exit holes are then plasma-etched through the boron-doped layer. Next, in the most critical step, a sacrificial oxide is grown using dry thermal oxidation. The thickness of this layer, which can be controlled to ± 1 nm, will determine the channel dimension. Typical thicknesses are in the range 20–100 nm. Following the oxidation, a 2 μm , boron-doped polysilicon layer is deposited over the oxide. Another plasma etch is performed to produce the entry holes, the location of which is slightly offset from the position of the exit holes. The backside is then anisotropically etched in EDP solution to expose the membrane. Finally, the sacrificial layer is removed by selectively etching it with concentrated HF.

2.3. Fabrication of micromachined biocapsule

The biocapsule consists of two separate microfabricated membranes bonded together with the desired cells contained within the cavities (Figure 3) (Desai et al., 1998). The cavities containing the cells are bounded at the wafer surfaces by microfabricated membrane filters with well-defined pore sizes, to protect the cells from the larger molecules of the body's immune system.

Microfabricated biocapsules with membrane pores in the tens of nanometer range seem suitable for application in xenotransplantation. The typical dimension of insulin,

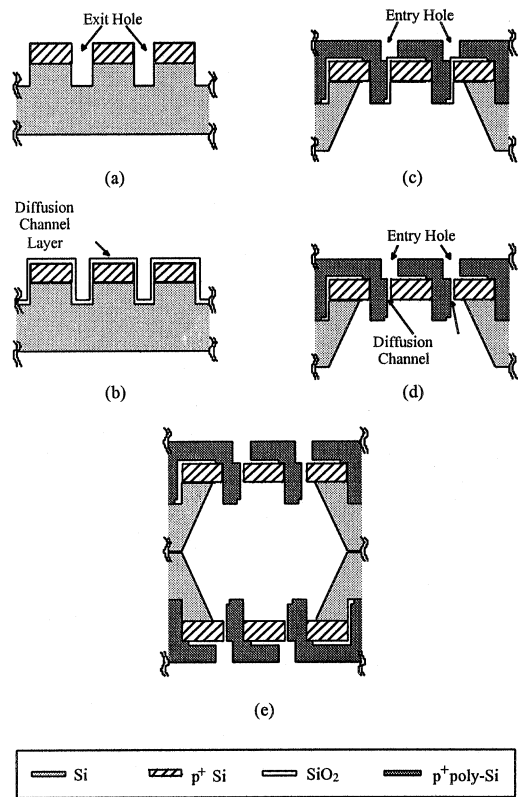


Fig. 3. Essential fabrication steps for the microfabricated biocapsule (not to scale).

glucose, oxygen and carbon dioxide, molecules which should pass freely through the membrane, is less than 35 \AA . The blockage of immune molecules, however, is a much more complicated task. Although it is relatively easy to prevent the passage of cytotoxic cells, macrophages, and other cellular immune molecules through the biocapsule, a potentially more serious problem is blockage of humoral immune components. These include cytokines, lymphokines, and antibodies. Antibody binding to a cellular transplant, by itself, usually does not cause a cytotoxic reaction. Moreover, it is the binding of the complement components that initiate the cytotoxic events (Lanza and Chick, 1995). Binding of C1q to IgM or two molecules of IgG can lead to the formation of a membrane attach complex (MAC) which will ultimately lyse the transplanted cell. Therefore, the immunoisolation membrane should prevent the passage of either host C1q or IgM to remain effective. Studies indicate that both C1q and IgG are completely retained by a membrane with maximum pore diameters of 30 to 50 nanometers (Lanza and Sullivan et al., 1992).

Nonetheless, it is not a simple manner of selecting an appropriate cut off dimension for the immunoisolation membrane. Permeability of glucose, insulin, and other

metabolically active products, must be high enough to insure therapeutic effectiveness. All previous immunoisolation membranes, due to their polymeric nature, have found that meeting these cut-off requirements is quite difficult, due to the broad pore size distribution of real membranes. Even if only 1% of pores are larger than the cut-off goal, the pores would allow the passage of antibodies in sufficient amounts to initiate immunorejection (Lanza and Chick, 1995). The technology involved in our microfabricated biocapsules is based on the creation of membrane with absolute and uniform pore sizes in order to better immunoisolate cellular transplants.

Although our proposed biocapsule was successfully fabricated, many challenges aside from fabrication were faced in the development of the capsule. Most importantly, interactions between the capsule and the cells contained in the capsule had to be characterized. It is necessary for the encapsulated cells to remain stable and viable in order to perform their intended metabolic function. Therefore, capsules are fabricated with pore sizes that are large enough for the timely diffusion of necessary cell nutrients and oxygen. Furthermore, the capsule should not elicit excessive inflammatory or chronic reactions from the host when in contact with the biological environment. Likewise, fibrotic encapsulation should not reduce pore patency below a limit of proper functionality.

One preferred biocapsule fabrication protocol is summarized here. The fabrication steps (Figure 3; not to scale) are: (a) A 4 in (100 mm) Si wafer is first boron-doped ($>10^{20} \text{ cm}^{-3}$). The etch area on the doped p+ silicon is photolithographically defined using a photo mask containing a $2 \mu\text{m} \times 2 \mu\text{m}$ array (Figure 2). $8 \mu\text{m}$ -deep exit holes are then etched through the boron-doped region. (b) A 20–100 nm sacrificial oxide layer (ultimately defines the diffusion channel) is deposited using dry thermal oxidation. (c) Anchor points are opened in the oxide and a $3 \mu\text{m}$ -thick boron-doped ($>10^{20} \text{ cm}^{-3}$) polysilicon layer is deposited. A final etch step is then performed to define entry holes in the polysilicon. (d) An EDP (ethylene diamine-pyrocatechol) etch is used to open the back side and form a half-capsule. EDP will selectively etch silicon without attacking the boron-doped silicon and polysilicon layer, or the oxide. Following the etch, the diffusion channels, defined by the oxide layer, are opened up with 5:1 buffered hydrofluoric acid. (e) Two half capsules are bonded together with polydimethyl siloxane to achieve the full biocapsule (Figure 3). The final biocapsule dimensions are: $1100 \mu\text{m}$ in thickness, 4 by 4 mm in lateral dimensions, membrane area of 10.4 mm^2 , cavity volume of approximately $10 \mu\text{l}$, and a membrane thickness of $9 \mu\text{m}$ (Figures 4 and 5).

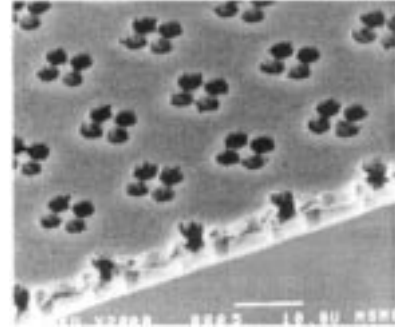


Fig. 4. Micrograph of top surface of biocapsule membrane.

Islet loading. Isolated islets are suspended in an alginate matrix (2%) to keep cells evenly dispersed. This suspension is gently pipetted into a half-capsule and joined by another half-capsule by an adhesive (medical grade silicone elastomer) to form the full capsule. Prior to use, biocapsules are stored in culture dish wells under appropriate culture conditions (incubation at 37°C , 5% CO_2 , in 1 ml of RPMI complete medium + 10% Fetal Bovine Serum).

Bonding. One major challenge associated with the microfabricated biocapsule is the procedure for bonding the two half capsules together. Due to the close proximity of cells and living tissue to both the internal and external capsule interface, the choice for a suitable bonding agent is nontrivial.

Because the cells are placed in the biocapsule before the pieces are bonded together, the bonding process must be able to occur in the presence of the biological materials to be transplanted without affecting their functionality (Hansford, 1996). While research has been performed extensively on adhesives that can be used in biological conditions, especially for dentistry and surgery (Tesk, 1989), there has been little work done on bonding techniques that are specifically non-cytotoxic

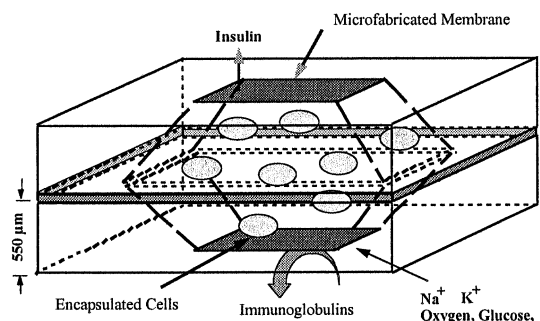


Fig. 5. Schematic of assembled biocapsule consisting of two micromachined membranes bonded together to form a cell-containing cavity bounded by membranes.

during the application and curing process. Additionally, the introduction of silicon as the biocapsule material increases the limitations of the bonding technique employed. The surface chemistry of silicon is quite different from traditional biomaterials and therefore, a biocompatible bonding agent for silicon is not necessarily readily available, nor thoroughly investigated.

The microelectronics industry has studied adhesives for standard silicon processing, as needed for the packaging of ICs and multi-chip modules (MCMs). However, the conditions for bonding in these applications is not similar to those needed for biohybrid devices. In addition to typical mechanical requirements, including the strength of the bond, the resistance to shear stresses (capsules in the body are subjected to minimal tensile stresses), there are several additional constraints in biomedical applications. Important parameters such as bonding temperature, residual solvents, outgassing, degradability, impermeability, and chemical composition must be taken into consideration when choosing an appropriate bonding agent for our biocapsule.

In our *in vitro* studies with fully bonded micro-fabricated biocapsules, the bonding agent used was a medical grade silicone elastomer (Type A Medical Adhesive, Factor II Inc.). However, because this is not an ideal bonding agent, studies have been and are currently being performed on the suitability of other bonding alternatives including industrial grade silicone, medical grade silicone, PMMA, PPMA, and PEMBA. The materials investigated were selected because of their processing temperatures, their previous use (or previous use of materials similar to them) as adhesives, and other qualitative factors (e.g., response to initial testing). Most other traditional materials that have been used to bond silicon wafers are not acceptable due to their processing temperatures, outgassing problems, or presence of other potentially cytotoxic substances. Other biomedical adhesives were not suitable due to difficulty in handling or cytotoxicity.

The results obtained from both mechanical and cytotoxicity testing show that either of the lower T_g methacrylates (PPMA and PBEMA) investigated could make suitable bonding agents for the microcapsules. Their non-cytotoxicity is clearly sufficient for use in the presence of live (Hansford et al., 1998). They both have been used to bond silicon at body temperature (by pressing two pieces of silicon, one coated with the polymer, together between the hands of the investigator), but at that temperature defects become highly relevant. Preliminary studies have also shown that bonding at higher temperatures would be possible. It was found that bringing the polymer-coated silicon in contact with the filled wafer at a higher temperature (70°C) only raises the temperature of liquid in another silicon cavity by 45°C.

Other studies have also shown that even highly sensitive cells can survive temperatures as high as 45°C for periods up to two minutes (Craig, 1993).

Mechanically, the methacrylates have shown that once properly bonded, they have more than sufficient strength for use in the body. By comparison, PPMA and PBEMA have higher adhesive strengths than PMMA, which is currently used as a bone cement, perhaps one of the most demanding mechanical applications of biomaterials to date. The small size of the devices also greatly limits the stresses that can be experienced, lowering the adhesive requirements well below the strengths of most bonding processes.

2.4. Encapsulated channel nanofilter

We have also created an alternative filter structure that may be more suitable for high-pressure applications in bioseparation. The encapsulated channel filter consists of two bonded silicon wafers: the micromachined filtration structural wafer and the cap wafer (Figure 6). Fluids enter through the hole etched in the cap wafer, then flow horizontally through the filtration channel as defined by the gap between the cap wafer and the machined features on the structural wafer, and then out the hole etched in the structural wafer. The channel height determines the nominal pore size. To enhance the flux, an interdigitated finger geometry is used (Figure 7). In this design, the effective pore surface area and consequently the porosity is dependent on the number, length, and width of the channel ridges, the width and periodicity of the anchor points, and the channel height. By changing these geometric parameters, the filter's flux (volume per area-time) can be optimized (Chu et al., 1996).

Using a finger width of 20 μm , a channel ridge width of 5 μm , a nominal pore size of 40 nm, and an operating pressure of 20 psi, effective fluxes of 108 l/cm²-hr and 161 ml/cm²-hr have been attained for N₂ and phosphate buffered saline, respectively. Filtration studies using fluorescent beads suspended in either PBS or ethanol have shown that filters with a nominal pore size of 40 nm can achieve >99.99% filtration of 100 nm and larger

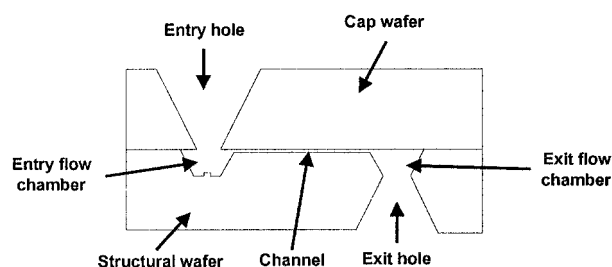


Fig. 6. Cross-sectional view of encapsulated channel filter.

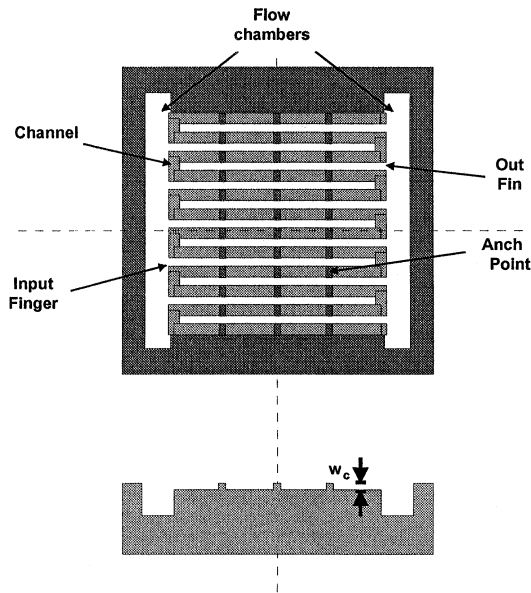


Fig. 7. (a) Top view and (b) cross-sectional view of structural wafer. The dashed horizontal line is through a channel ridge.

beads and 99.3% filtration of 44 nm beads. The slight decrease in retention of 44 nanometer beads is thought to be a result of several factors including dye leaching from the beads, bead size variation, and possible membrane defects. Since flow is through encapsulated channels, this filter embodiment is more mechanically robust than a membrane structure, and is particularly well suited for large volume, high-pressure applications.

The fabrication of the encapsulated channel filter uses a bulk micromachining process, in which all the structural layers are formed in the starting silicon wafer. The processing can be broken into three steps: (1) Structural wafer processing, (2) Cap wafer

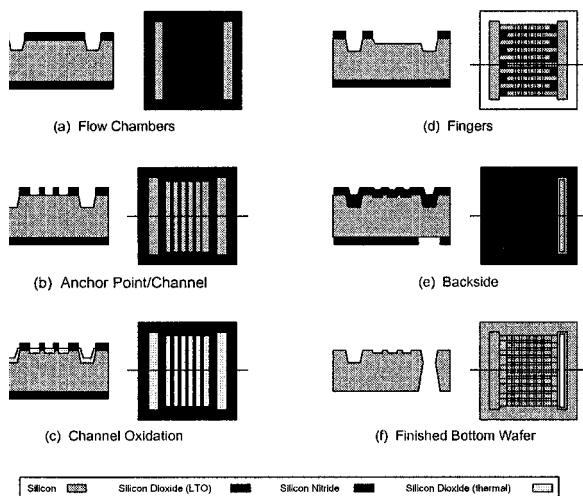


Fig. 8. Process flow for filter membrane.

processing, and (3) Wafer bonding. Unless stated otherwise, a freshly grown, low-temperature oxide (LTO) is used as the mask layer for the various photolithography steps. In the first step (Figure 8a), 2 μm -deep entry and exit flow chambers are etched into the silicon with a 33 wt% Potassium Hydroxide (KOH) solution. For the next lithography step, a low-stress silicon nitride layer (on top of a pad oxide) is used as the mask layer because it has good oxide masking properties. First, the nitride is patterned to define the anchor points, and then the exposed silicon is selectively oxidized to form the sacrificial layer. This sacrificial layer will eventually determine the channel dimension. Of interest is not the total thickness, but the amount of silicon that is consumed during the dry oxidation step. Using the fact that thermal oxidation consumes the underlying silicon at a rate of 44% of the total oxide thickness, an oxide layer is grown such that when it is removed, a pocket will be produced in the silicon, with a depth equal to the desired channel height. With this technique, thickness variation can be controlled to ± 1 nm across a 4-inch wafer. Following the channel formation, the wafer is stripped clean of any nitride and oxide layers and prepared for finger patterning (Figure 8d). Again, using a 33 wt% KOH solution, inlet and outlet fingers are etched into the silicon to a depth of 2–6 μm . Finally, an ethylene diamine-pyrocatechol-pyrazine (EDP) etch is performed on the backside to make a through-hole connection to the exit flow chamber. For the cap wafer, a lithography step followed by an EDP etch is used to form a through-hole that will eventually line up to the entry flow chamber on the structural wafer. After both the structural and cap wafers have been processed, the wafers are then thoroughly cleaned, in succession, with piranha (1:4 H_2O_2 : H_2SO_4), concentrated hydrofluoric acid HF, RCA-1 etch (1:1:4 NH_4OH : H_2O_2 : H_2O), and deionized H_2O . After spin drying, the cap wafer is aligned over the structural wafer, and direct-bonded. A nitrogen anneal is then performed at 1000°C for 2–4 hours to strengthen the bond.

3. Biocompatibility of Nanomembrane and Biocapsular Environment

Our preliminary studies centered upon investigating the general biocompatibility of silicon membranes. Direct cell contact tests and long-term bulk material implants indicated a sufficient degree of long-term (Desai et al., 1995). It has also been established qualitatively that anchorage dependent cells can grow normally on flat

silicon microstructures (Lassen et al., 1992; Richter et al., 1996) and that microfabricated environments can be bioactive (Calhan, 1995). We qualitatively investigated the functionality of cells in three-dimensional configurations of microfabricated silicon environments, with varying pore sizes in the micro- to nanometer range, in order to more closely simulate a biocapsule environment. This behavior of different cell types in three-dimensional silicon microstructures was studied using microfabricated half-capsules (or culture wafers), as described below.

For the silicon membranes, preliminary biocompatibility and cytotoxicity tests have been performed by examining the cell morphology, growth, and function of test cell lines placed in contact with arrays of membranes (Figure 9), with promising preliminary results. The biocompatibility was evaluated via direct contact tests by cultivating several different cell lines such as macrophages, fibroblasts, and HeLa cells, as well as isolated primary islets of Langerhans both on the wafer surface and within the porous wafer pockets (Ferrari et al., 1996). All cells were seeded on silicon culture wafers, observed via light microscope, stained for cell viability and functionality, and counted with a hemacytometer. All cell types had normal growth characteristics, morphology, and greater than 90% viability (Figure 10).

In previous studies, cell functionality has also been studied in microfabricated silicon three-dimensional permselective environments, with varying pore sizes in the micro- to nanometer range. Evaluating antibody secretion from hybridomas and insulin secretion from rat islets of Langerhans (Ferrari et al., 1996) monitored cell functionality. The level of antibody secretion from hybridomas cultured on silicon membranes and in control polystyrene culture wells was similar by western blot analysis, indicating no apparent impairment of hybridoma function in the culture wafer pockets. Overall, islets in microfabricated silicon pockets and the control dishes appeared to have similar morphology and viability. Glucose-supplemented medium was allowed to diffuse to the islets, from underneath the membrane, to stimulate insulin production and monitor cell functionality. Similar levels of insulin secretion were measured for islets within microfabricated cell culture arrays and

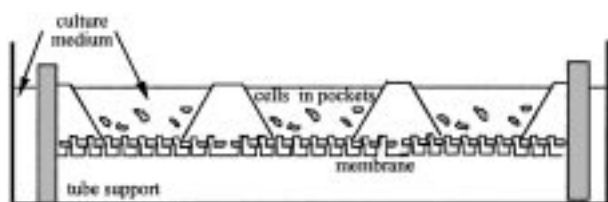


Fig. 9. Cells cultured in arrays of membrane-bounded wells.

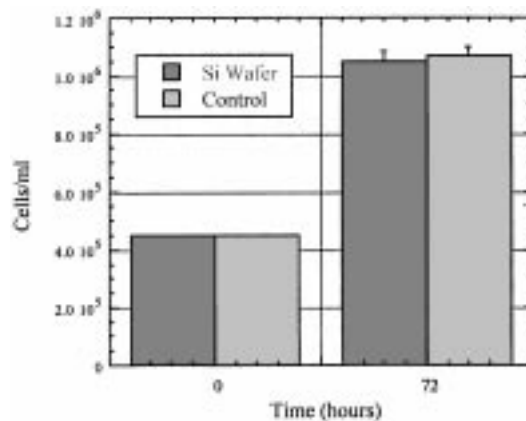


Fig. 10. Cell growth on Si culture wafer.

on control surfaces suggesting that glucose was able to sufficiently pass through the pores of the wafer pockets to stimulate islets for insulin production. The environment of the silicon pockets showed no inhibition of islet functionality and insulin secretion, as compared to control islets (Desai et al., 1998).

In vivo biocompatibility of silicon microimplants. In vivo, the biocompatibility of silicon microimplants was evaluated by implanting square block samples (3 mm × 3 mm × 0.5 mm) into the pancreas, liver, spleen and kidney of adult (Craig, 1993). Specimens were fabricated either with 2 mm blind filtration channels cut into the central portions of silicon blocks coated with polysilicon or single crystal silicon blocks with no polysilicon coating. For both groups of silicon microimplants, the surface appearance was the same both before and after the implantation. There appeared to be no changes in the mechanical properties of the implants and no corrosion was observed. The surface of the samples remained smooth although some of the wafers displayed slight tissue adherence. The blind filtration channels appeared clear and free from any obstructions.

The tissue response to the implants was assessed by light microscopy by a modification of the method developed by Salthouse (Salthouse and Matlaga, 1975). No significant differences were observed between the two implant types in terms of chronic tissue response. Although a fibrous tissue capsule was maintained by the continuing presence of the implant, the surrounding tissue appeared normal and well vascularized. No gross abnormalities of color or consistency were observed in the tissue surrounding the implant. In general, the fibrous capsule was well-formed and displayed little migration. No necrosis, calcification, tumorigenesis, or infection was observed at any of the implant sites. Overall, our biocompatibility studies suggested that silicon substrates

were well-tolerated and non-toxic both *in vitro* and *in vivo*, leading to our further studies on islet encapsulation within biocapsules.

Islet functionality studies. In collaboration with Dr. Alberto Hayek and Gillian Beattie of the Whittier Institute for Diabetes in San Diego, California, prototype microfabricated biocapsules were tested using isolated neonatal rat pancreatic islets of Langerhans (Desai et al., 1998). First, the viability and functionality of islets within the porous pockets of the microfabricated *culture wafer* were monitored *in vitro*. Then, the stimulus-response function of islets within *fully-assembled* biocapsules was studied.

Viability of islets in culture wafers/half capsules. The morphological state of pancreatic islets, placed in microfabricated culture wafer pockets, were examined daily. Overall, pancreatic islets in the silicon pockets and the control dishes appeared to have similar morphology. The islets were all intact and round in appearance. Islets in pockets showed less dissolution or dissociation than islets in standard culture dishes. Islets in both the culture wafer pockets and standard culture dishes exhibited slight necrosis in their central portions after 72 hours.

Cell functionality and membrane permeability to glucose and insulin. The ability of pancreatic islets of Langerhans to secrete insulin in response to glucose diffusion through capsule pores was first studied in both microfabricated half-capsule environment. Islet cells were cultured in the pockets of silicon culture wafers with pore sizes of 78 nm, as well as in standard culture dishes as controls.

Membranes of 78 nm pore size were used for the initial rounds of testing—a dimension which could easily be modified and optimized later. Glucose-supplemented medium was allowed to diffuse to the islets, from underneath the membrane, to stimulate insulin production. The concentration of insulin, secreted by the islets through the membrane, into the surrounding medium was compared between the unencapsulated islets and the islets in 78 nm pore-sized half culture wafers. The insulin concentration for half culture wafers was comparable to the unencapsulated islets, suggesting that glucose was able to sufficiently pass through the pores of the wafer pockets to stimulate islets for insulin production. It appears that the environment of the silicon pockets does not impede islet functionality and insulin secretion, as compared to unencapsulated islets. Figure 11 shows the secretion of insulin for control and half-encapsulated islets at 24 and 72 hours.

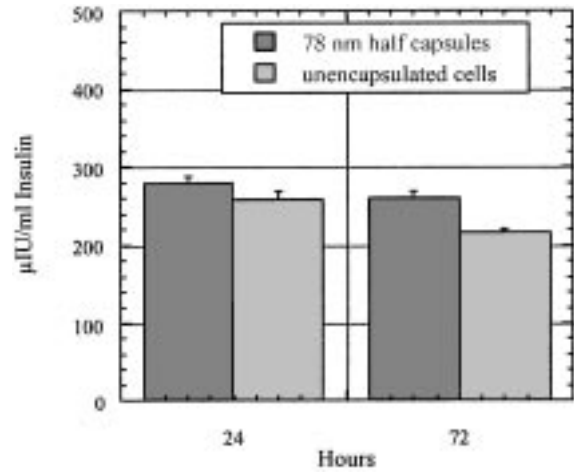


Fig. 11. Insulin Secretion at 24 and 72 hours.

Studies with full biocapsules. Cell functionality studies have also been conducted with islets within fully assembled biocapsule, as reported previously (Desai et al., 1998). Full capsules were obtained by joining two half-capsule units containing islet-prefilled pockets. Performance was again monitored by measuring insulin concentration after glucose stimulation of the capsules in cell culture medium. Results indicated that secretory response is similar to unencapsulated islets, with insulin release occurring within ten minutes of stimulation (Figure 12). Experiments examined the viability of islet clusters within the microfabricated biocapsule. As seen in Figure 13, fully encapsulated islets remain viable and functional as long as control islets. Because rat pancreatic islets of Langerhans are primary mammalian cells, they have a finite lifespan *in vitro*, typically less than six weeks. Our biocapsule studies, therefore, indicated that the microfabricated

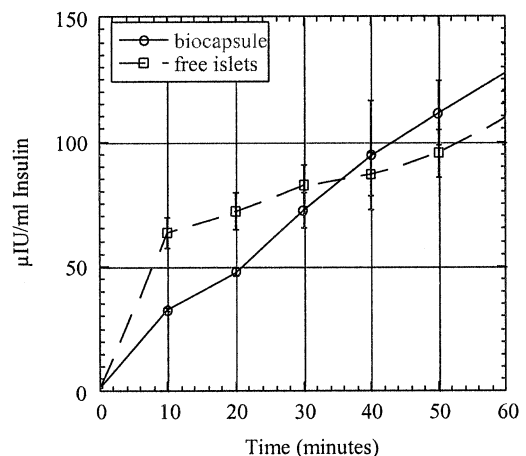


Fig. 12. Insulin secretory rate for islet-filled biocapsule.

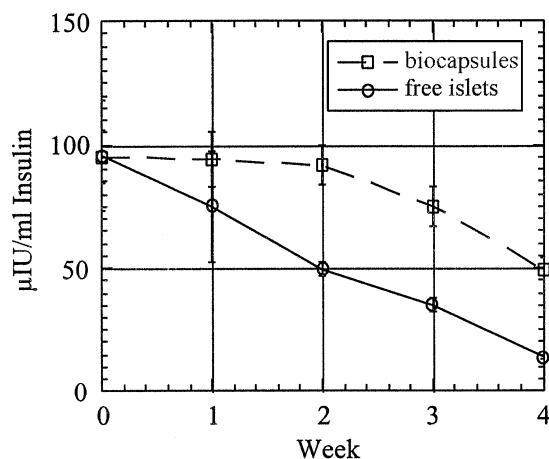


Fig. 13. Insulin secretion over one month.

environment is not detrimental to the islets and may actually prolong lifespan *in vitro*.

Anti-fouling protocols. Fouling is perhaps the most important issue that needs to be addressed in our filter designs, especially in regards to biological systems. It has recently been shown that stable bioinert polymer chains attached to the silicon surface can reduce the protein adsorption (Piehler et al., 1996). In view of the potential applications of the nanoporous membranes, novel methods for the grafting and characterization of protein-resistant coatings have been recently developed based on solution (Zhang and Ferrari, 1997; Zhang et al., 1998) and vapor phase coating methods (Wang and Ferrari, 1998). Both of these methods will be discussed in detail later.

Diffusion studies (Desai et al., 1999).

Initial diffusion studies were carried with polystyrene beads of various dimensions in a diffusion chamber as shown in Figure 14. It was found that biocapsules membranes of 18 nm pore size completely blocked the

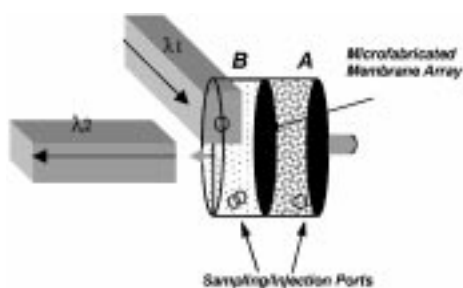


Fig. 14. Rotating diffusion chamber used to test microfabricated membranes.

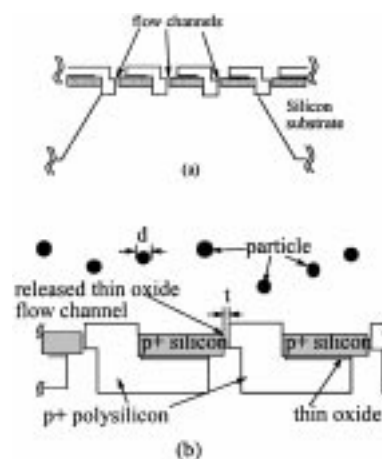


Fig. 15. Schematic of (a) microfabricated multifunctional membrane design and (b) permselectivity based on size, shape, and/or charge.

diffusion of 44 and 100 nm diameter polystyrene beads, while 66 nm pore sized membranes only blocked 100 nm diameter beads. No fluorescent signal above baseline was detected in the incubation medium surrounding 18 nm biocapsules after 1 and 4 days. This suggests that the biocapsule achieved absolute retention of the beads (Figure 15).

Glucose and insulin diffusion. The concentration of insulin, secreted by the islets through the membrane, into the surrounding medium was compared between the unencapsulated islets and the islets on micromachined membranes. The concentration of diffused insulin through the membrane into the medium was compared to the amount of insulin secreted by unencapsulated islets. The amounts were similar in concentration and time release suggesting that glucose was able to sufficiently pass through the pores of the wafer pockets to stimulate islets for insulin production.

Results indicated that the insulin secretion by the islets and subsequent diffusion through the biocapsule membrane channels was similar to that of unencapsulated islets for both 3 micron and 78 nm pore sized membranes, with insulin diffusion through the membrane occurring within ten minutes of stimulation. Figures 16 and 17 show the typical insulin release profile in response to stimulatory (16.7 mM) glucose medium over 1 hour under static incubation for 78 nm, 66 nm, and 18 nm pore-sized membranes. This profile indicated that insulin and glucose diffusion occurred at sufficiently high rates through the microfabricated membrane to ensure nutrient exchange for encapsulated islet cells. These experiments show that no diffusion barrier is formed by the membrane for glucose and insulin, while taking into account the effect of rotation on mass transfer.

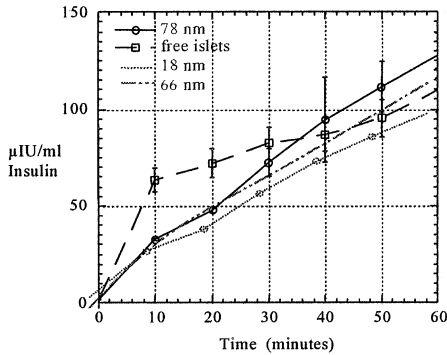


Fig. 16. Insulin secretory profile through differing pore sizes.

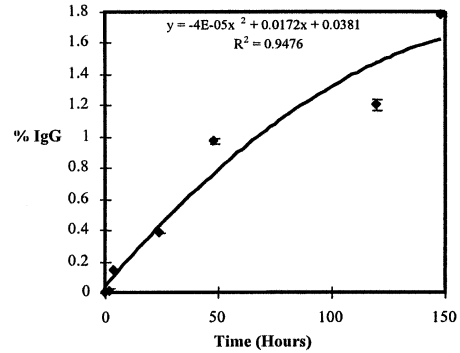


Fig. 18. Diffusion of IgG through 18 nm pore-sized membrane.

IgG diffusion. The data indicated that microfabricated biocapsule membranes could be tailor-made to attain desired IgG diffusion kinetics. At the same time, the complete deselection of IgG requires absolute pore dimensions below 18 nm. This refines the previous understanding that pore in the range 30–50 nm would suffice to provide membrane-based immunoisolation (Lanza et al., 1992). With reference to the data reported in Figures 17–18, it is noted that the percent of IgG diffusion (concentration of IgG that passes through the membrane) was less than 0.4% after 24 hours and 2% after over 150 hours through the 18 nm membranes (F. Compared to commonly used polymeric membranes, this rate was several times smaller indicating superior immunoprotection. For example, Dionne et al. (1996) measured an IgG concentration of 1% after 24 hours through poly(acrylonitrile-co-vinyl chloride) membranes with a molecular weight cut-off of $\approx 80,000$ MW. Although the IgG molecule has a molecular weight of approximately 150 kD, studies have disagreed on the actual dimensions of the molecule, estimated to be tens

of nanometers or less. For example, Wang and colleagues (1997) investigated permeability of relevant immune molecules to sodium alginate/poly-L-lysine capsules and found that significant amounts of IgG (close to 40%) passed through both 230 kD and 110 kD membranes in 24 hours (Wang et al., 1997).

Islet immunoprotection. As shown in Figure 19, the 18 nm biocapsules seem to provide significant immunoprotection to those islets encapsulated within its semi-permeable membrane. After two weeks in culture with antibodies and serum complement, islets in microfabricated biocapsules maintained close to original glucose stimulated insulin secretory capability even after two weeks in the presence of antibodies and complement. Islets immunoprotected by 18 nm pore-sized membrane maintained their functionality better than those in 78 nm pore sized biocapsules, confirming that greater immunoprotectiveness was offered by 18 nm membranes. In contrast, there was a marked decrease in baseline and stimulated response in free islets.

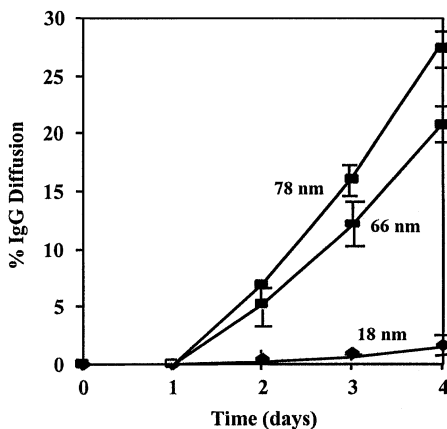


Fig. 17. IgG diffusion through microfabricated biocapsules of three different pore sizes.

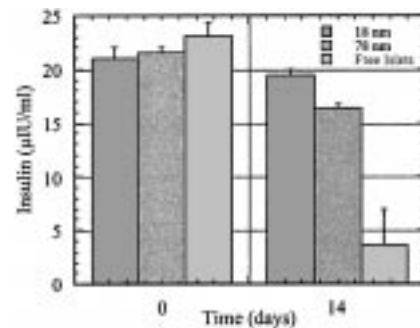


Fig. 19. Insulin secretion of islets within different pore-sized biocapsules and unencapsulated incubated for two weeks with serum complement/antibody solution (20 islets/biocapsule, n = 6).

Studies on the short-term immunoisolation of insulinoma xenografts (Desai et al., 1998a; Desai et al., 1998b)

In vitro static incubation study. Microfabricated biocapsules incubated *in vitro* for eight days showed stimulus secretion coupling of glucose and insulin for encapsulated insulinoma cells (Table 1). As shown in Figure 20, the static incubation study resulted in insulin secretion from the microfabricated biocapsules containing RIN cells in response to basal glucose levels and stimulatory glucose (2.8 mmol/L) levels. The stimulatory index (SI = stimulatory/basal insulin secretion) in picograms (pg) for RIN cells in 18 nm pore-sized microfabricated biocapsules was approximately 1.7. In 66 nm pore-sized biocapsules, the basal value was 12.0 ± 5.65 and jumped significantly to 71.3 ± 17.25 under stimulatory conditions, an almost 6-fold increase. Similarly, encapsulated β TC6F7 cells also displayed basal and stimulatory (16.7 mmol/L) insulin release, with a SI of 4.3 for 18 nm pore-sized biocapsules. Biocapsules of 66 nm pore-size containing β TC6F7 cells had a SI value of 9.1 *in vitro*.

In vivo study. After eight days of intraperitoneal implantation, glucose stimulated insulin secretion from the retrieved biocapsules was examined under static

Table 1. Insulin secretion from glucose stimulated biocapsules where SI = stimulatory index (stimulatory insulin secretion over basal insulin secretion)

| Cell | | SI (18 nm) | SI (66 nm) |
|---------------|-----------------|----------------|---------------|
| RIN | <i>In vivo</i> | 1.5 ± 0.4 | 1.7 ± 0.2 |
| | <i>In vitro</i> | 1.9 ± 0.05 | 5.9 ± 0.9 |
| β TC6F7 | <i>In vivo</i> | 3.6 ± 0.3 | 1.7 ± 0.2 |
| | <i>In vitro</i> | 4.3 ± 0.7 | 9.2 ± 0.5 |

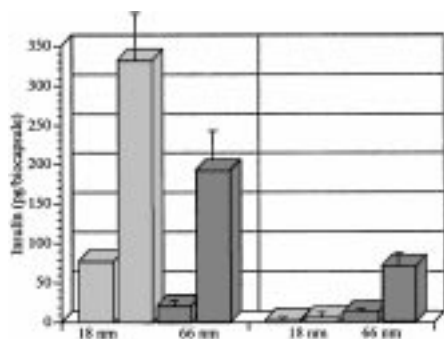


Fig. 20. In vitro insulin secretion from RIN and β TC6F7 filled biocapsules in response to basal and stimulatory glucose levels. Mean values are expressed in picograms insulin released (\pm SD) per 18 nm or 66 nm pore sized biocapsule.

conditions. Microfabricated biocapsules were easily located in the abdominal cavity of laparotomized mice. Three biocapsules remained in the original implantation site, while the remaining biocapsules migrated to either the abdominal cavity, bowel loops, or mesentery. Nonetheless, all biocapsules seemed mechanically intact with no macroscopic changes in surface architecture or properties. Tissue surrounding the biocapsules found in their original implantation site showed no abnormalities while tissue around two of the migrated biocapsules displayed minor neutrophil infiltration. This could reflect poor surgical implantation or sterile techniques. Some capsules ($n = 4$) had agglutinated during their migration but were mechanically intact nonetheless.

In vivo, the β TC6F7 cells remained viable in microfabricated environments. The stimulatory index for 18 nm and 66 nm pore size microfabricated biocapsules was 3.6 and 1.75, respectively. The xenogeneic RIN cells encapsulated in 18 nm biocapsules were also able to maintain their functionality and displayed basal and stimulatory insulin secretion of 2.23 ± 1.12 and 3.10 ± 0.5 , corresponding to a stimulatory index of approximately 1.5. In 66 nm pore sized biocapsules, RIN cells had a stimulatory index of approximately 1.7. In contrast, the freely injected RIN and β TC6F7 cells were undetectable in the peritoneum as well as in any other organ (liver, kidney, lungs, or brain) as determined by careful autopsy. The peritoneum is known to elicit a strong immune reaction to these free insulinoma cells. Viable free insulinoma cells are expected to form a tumor nodule. However, it was nonetheless observed that all 2×10^5 free insulinoma cells were completely taken up by the immune system while encapsulated insulinoma cells survived and maintained functionality (Figure 21).

Several issues regarding microfabricated biocapsule implantation and effectiveness were revealed in these

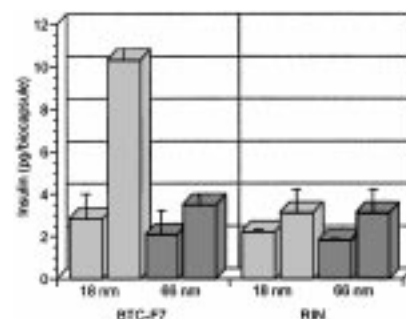


Fig. 21. Insulin secretion from RIN and β TC6F7 filled biocapsules in response to basal and stimulatory glucose levels after 1 week intraperitoneal implantation. Mean values are expressed in picograms insulin released (\pm SD) per 18 nm or 66 nm pore sized biocapsule.

experiments. Insulinoma cells did maintain their viability within microfabricated biocapsules over the studied period. However, it was shown that encapsulated β TC6F7 cells *in vitro* maintained a greater stimulatory insulin response than *in vivo*. Also, the size of the pores of the biocapsule greatly affected the secretory response. The lower insulin response in the 66 nm biocapsules implanted compared to the implanted 18 nm biocapsules could be attributable to the penetration of immune molecules through the relatively larger membrane pores and subsequent attack of encapsulated insulinoma cells. The effective size of antibody and complement components of the immune system has been hypothesized to be between 20 and 50 nm (Colton, 1995). Previous studies on biocapsules have suggested that pore sizes smaller than 100 nm are effective in hindering passage but still do not completely block immune molecules from reaching the target cell (Colton and Avgoustiniatos, 1991). Therefore, it is likely that a pore size of 66 nm still allows passage of immune molecules. Comparing the stimulatory indices of β TC6F7 cells in 18 and 66 nm pore-sized capsules *in vitro*, we find that the indices are approximately 4 and 9, respectively (Table 2). This suggests that the larger pores of the 66 nm capsules are more effective in facilitating nutrient diffusion to the encapsulated cells, leading to greater cell viability. This behavior is echoed in the case of RIN cells *in vitro*, where indices are approximately 2 and 6 for 18 and 66 nm biocapsules, respectively.

Turning to the explanted biocapsules, we observed stimulatory indices of approximately 4 and 2 for β TC6F7 cells in 18 and 66 nm pore-sized capsules, respectively (Table 2). Similarly, RIN cells in explanted 18 and 66 nm pore-sized capsules both had indices of approximately 2. We observed that a sharp reduction in the stimulatory indices of both cells lines in 66 nm biocapsules, whereas the stimulatory indices of explanted 18 nm capsules remains essentially the same as that which was observed for *in vitro* 18 nm biocapsules (Table 2). This seems to indicate the immunoisolatory effect of 18 nm pore-sized biocapsules and the lack of effective immunoisolation by the 66 nm biocapsules.

It is significant to note that there is a reduction of stimulatory index between *in vivo* and *in vitro* capsules.

Table 2. Percent decrease in encapsulated cell insulin secretion (explanted/incubated) in microfabricated biocapsules

| | Per cent decrease in insulin secretion between incubated and explanted biocapsules | |
|---------------|--|----------------|
| | 66 nm capsules | 18 nm capsules |
| RIN | 66 | 22 |
| β TC6F7 | 88 | 14 |

The decrease in levels of insulin secretion in the explanted biocapsules, compared to the incubated biocapsules is associated, in part, with a certain amount of shock induced in the implanted cells. The fact that 66 nm pore-sized capsules had a greater reduction in levels of insulin secretion than 18 nm capsules points to a scenario of negative feedback and shock, but *not* pore clogging, since one would expect bigger pores to clog less than smaller ones. This is also supported by the observation that both cell lines in implanted biocapsules had a decrease in insulin secretion compared to *in vitro*, despite the differences in immunogenicity. Since this was a short term study, the implanted cells may not have had a sufficient amount of time to adjust to their new environment and regain functional normalcy. These cells were then explanted and subjected to another change in ambient conditions, resulting in yet further stress. Such shifts in environment could easily account for lower insulin secretory capabilities.

Since the experimental animals were normoglycemic, already established mechanisms of insulin feedback control may have altered or negatively inhibited insulinoma homeostasis (Colton and Avgoustiniatos, 1991; Scharp et al., 1984). The implanted cells were augmenting and thus competing with fully-functioning pancreatic cells in terms of glucose-stimulated insulin secretion.

Additionally, perhaps the location and method of implantation could be improved. Biocapsules that did not migrate into lower body spaces seemed to perform better than those that did. If capsules themselves are placed in a larger sack or mesh to prevent movement or are anchored to tissue by suturing, this may improve performance and deter biocapsule adhesion to one another. Moreover, the rate of fibrosis seems to depend on the localization of the biocapsules. Limiting or preventing biocapsule displacement and migration will deter fibrotic capsule formation.

4. Bioengineering of the Microfabricated Surfaces

4.1. Protein resistance by physisorption and covalent immobilization of PEG/PEO

Significant control over protein adsorption and cell adhesion has been achieved in many biomaterials by the surface immobilization of polyethylene oxide (PEO) or polyethylene glycol (PEG), both nontoxic, protein-resistant, and non-immunogenic polymer film (Mrksich and Whitesides, 1996; Aldenhoff, 1995). The science and technology of PEG immobilization on polymeric surfaces have recorded major advances in the past decade (Beyer et al., 1996; Morpurgo et al., 1996).

Several techniques, including physical adsorption and graft polymerization by plasma and photo-induced coupling have been also introduced to coat PEG on glass (Strasser et al., 1989; Kamath et al., 1996; Tseng and Park, 1992). The PEG coatings deposited by the cited methods have proven successful in depressing protein adsorption and cell attachment. However, the thicknesses of these coatings limit their viability in applications where nanometer-scale dimensional requirements must be enforced in the field of BioMEMS. In this sense, it is necessary to develop and validate new methodologies in the control of protein adsorption on silicon surfaces by coating with PEG films at the molecular level.

For this purpose, we have developed two novel surface modification protocols. In the first approach, a polyethylene glycol (PEG) protein-resistant film is physically adsorbed on silicon surfaces. In the second approach, PEG protein-resistant films are covalently immobilized on silicon surfaces through a combination of organic synthesis and self-assembly. Surface coatings are characterized by contact angle measurement, ellipsometry, optical microscope, and electron spectroscopy for chemical analysis (ESCA). Adsorption of albumin, fibrinogen, and IgG to PEG immobilized silicon surfaces is studied by ellipsometry to evaluate the non-fouling and non-immunogenic properties of the surfaces. In both cases, coated PEG chains show the effective reduction of both plasma protein adsorption and cell attachment to the modified surfaces.

Physical adsorption of protein resistant (Zhang and Ferrari, 1997). In this approach, protein adsorption on silicon was tailored by preadsorbing surfactant Tween molecules on a hydrophobized silicon surface with their hydrophobic tails toward the adsorbing surface and hydrophilic proteins-resistant heads toward surface exterior. Silicon is hydrophobized by methylation and HF treatment.

The ability of Tween 20 to reduce the adsorption of albumin on silicon surfaces with different wettabilities was shown in Figure 22. A reduction of 90% in the albumin adsorption on most hydrophobic surfaces (contact angle 100°) by Tween 20 was achieved, whereas only a 5% reduction on hydrophilic surfaces (contact angle less than 10°) was obtained. The reductions of albumin adsorption on intermediate surfaces (contact angle about 60°) were 60%. HF treated surfaces are often encountered in microfabrication processes and are thereby of great importance to silicon nano-filters, biosensor, and most other microdevices. Silicon surface modification by HF treatment is very simple and can be finished within 5 min.

Experiments of time-dependent protein adsorption in

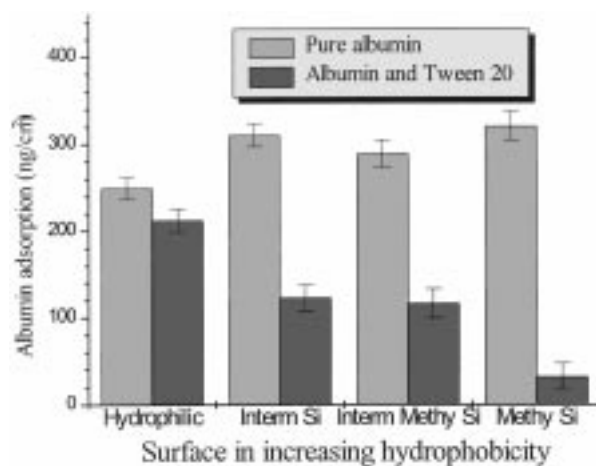


Fig. 22. Albumin adsorption on various surfaces from single protein and protein-surfactant mixture solution.

both pure protein and protein-surfactant mixtures were also conducted to ascertain the stability of physically adsorbed Tween 20 films. It was found that the adsorbed Tween 20 film was robust and there was no evidence of exchange of the Tween molecules with albumin within our test period of time.

Covalent immobilization of protein resistant films by self-assembly (Zhang et al., 1998; Zhang and Ferrari, 1998a; Zhang and Ferrari, 1998b). In this approach, PEG is chemically coupled on silicon through the functionalization of a PEG precursor by the formation of SiCl_3 groups at its chain ends, followed by the reaction of surfaces with compounds of PEG-OSiCl_3 (Figure 23). A monolayer by strong chemical bonds is self-assembled on the surface. A PEG monolayer provides a terminal hydroxyl group that could construct another monolayer on its surface. A self-assembled multilayer can be built by the repetition of this process. The thickness of the

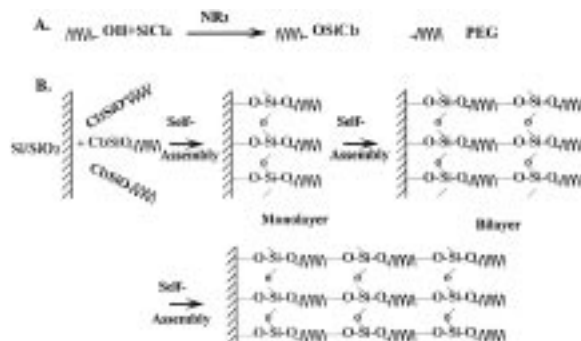


Fig. 23. Schematic of immobilization of PEG on silicon.

multilayer of the PEG film is controlled by silanization time.

Surface characterization. Figure 24 shows the spectra of high resolution of the carbon 1s region of the unmodified (a) and PEG immobilized silicon (b) surfaces. In the spectrum, the major peak of the unmodified surface centers near ~ 285 eV, corresponding to carbon-hydrogen binding energy. The major peak of the spectrum of the PEG-modified silicon surfaces centers at 286.3 eV, in accord with the standard C_{1s} binding energy (286.4) of PEG (Beaman and Briggs, 1992). This supports the success of immobilization of PEG film on the silicon surface.

The spectra of high resolution of the Si_{2p} region of the unmodified (a) and PEG modified (b) silicon substrates are presented in Figure 25. After coating, the silicon peak was decreased while the silicon oxide peak was increased. This suggests the presence of $-O-Si-O-$ bond and the formation of replicative PEG-siloxane crosslinked structure. The binding energy of silicon oxide shifted from 103.4 to 104.5 eV. It is known that a chemical shift varies measurably with change of chemical environment and the crosslinked siloxane bond films have a larger binding energy than native silicon dioxide (Brundle et al., 1992). Therefore, our results strongly support the formation of the proposed structure of the PEG cross-linked polymer network, as illustrated in Figure 4 (b).

Enhancement of silicon hemocompatibility. The time dependence of albumin, fibrinogen, and IgG adsorption on unmodified and modified silicon surfaces is shown in Figure 26. Adsorption on modified surfaces reached a maximum after approximately 60 minutes for all three of the proteins under investigations. By contrast, adsorbed

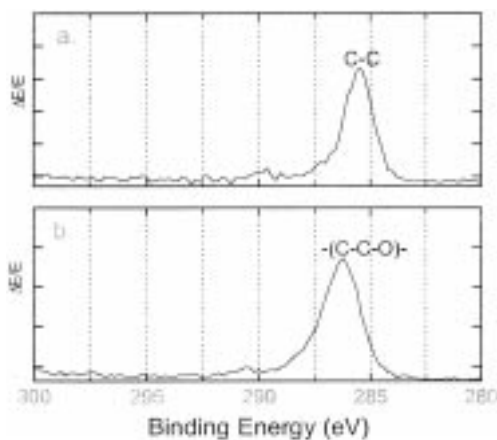


Fig. 24. XPS high resolution spectra of the carbon 1s for silicon (a) and PEG coated silicon (b) surfaces.

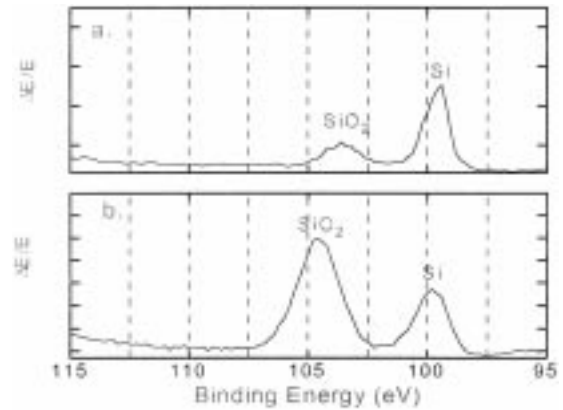


Fig. 25. XPS high-resolution spectra of the silicon 2p for silicon (a) and PEG coated silicon (b) surfaces.

amounts on unmodified surfaces increased monotonically in the time interval considered. Precoating silicon surfaces with PEG led to a marked reduction of protein adsorption. The reduction of albumin, fibrinogen, and IgG adsorption on PEG modified surfaces at 120 minutes were about 75%, 65%, and 80% (Zhang and Ferrari, 1998).

Platelet adhesion to unmodified and PEG modified silicon surfaces is shown in Figure 6. It can be seen that the PEG film severely limited platelet adhesion. Upon morphological examination, platelets on PEG are seen to present mainly the discoid shape that characterizes their inactivated status. By contrast, platelets on unmodified silicon exhibit pseudopods, as typically the case upon their contact with a thrombogenic surface. Reduced

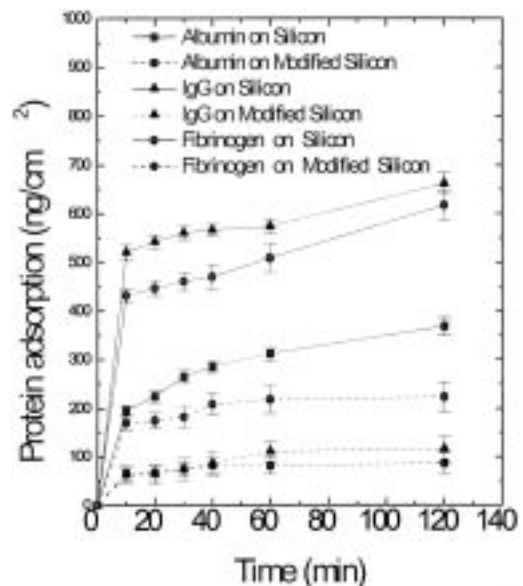


Fig. 26. Adsorption of albumin, fibrinogen and IgG onto silicon and PEG modified silicon surfaces.

plasma protein adsorption and platelet adhesion indicate that PEG modified surfaces have improved silicon hemocompatibility.

Enhancement of silicon tissue biocompatibility.

Figure 27 shows the adhesion of fibroblast and HeLa cells to PEG treated and untreated silicon substrates with respect to time (Zhang et al., 1998). Cell adhesion and a subsequent increase in the number of attached cells on both surfaces increased with time. However, significantly less initial cell adhesion was observed on PEG coated surfaces for both cell types. These observations are consistent with the results of other investigations involving cellular interaction with the PEG modified polymeric surfaces (Hsuie et al., 1996).

The reductions in the adhesion and proliferation of fibroblast and HeLa cells increased with time and maximum values were about 55%–62%, with the exception of the slight decrease of the reductions at the last data point for each experiment. Reduced protein adsorption and cell adhesion indicate that PEG modified surfaces have enhanced silicon tissue biocompatibility.

4.2. Surface modifications using vapor phase coating and solution coating

Silicon surfaces exposed to air or water develop a native oxide layer with surface silanol groups. The silanol groups are ionizable in water:



In fact, silicon surfaces in water are similar to quartz surfaces which have a point of zero charge (PZC) around pH 2 to 3. At pH below 2 the surface is positively charged. At pH above 3 the surface is negatively charged. Thus at neutral pH the silicon surface in water is negatively charged. A charged surface creates a streaming potential in the fluid flow and also promotes protein adsorption. In order to facilitate the flow and minimize protein adsorption, a hydrophilic, neutral, and ultrathin (or monolayer) coating is desired on silicon filters. Previous studies have shown that grafted alcoholic groups can drastically reduce protein adsorption on the surface of contact lenses, glass membranes, and porous silica (Scott and Mowrey-Mckee, 1996; Langer and Schnabel, 1988; Schnabel and Langer, 1991; Ho et al., 1976). Therefore alcohol terminated surfaces are highly desirable on silicon filters and other silicon based biomedical devices. As indicated in Figure 28, we assembled vinyl or glycidoxo groups on silicon filter surface and then to convert them to alcoholic groups.

Currently the predominant method of surface silanization is to assemble the so-called “monolayer” alkylsilanes onto silicon surfaces in organic solutions (Wasserman et al., 1989; Ulman, 1996; Maboudian and Howe, 1997) using alkyltrichlorosilanes (denoted as RSiCl_3) or alkyltrimethoxysilanes (denoted as $\text{RSi}(\text{OCH}_3)_3$), where R is any desired functional group to be introduced into the coating. However, these precursor molecules are sensitive to moisture. The polymerization with trace water in the organic solution or its environment could lead to formation of multilayers and aggregates on silicon surfaces, which would clog up micron-sized channels. We have focused on vapor phase coating of alkyltrichlorosilanes and alkyltrimethoxysilanes on silicon wafers and filters using nitrogen as a carrier gas, as compared with solution coating. The filters were tested with different fluids before and after the vapor phase coating.

Compared with solution coating, the vapor phase coating possesses the following advantages for the surface modification of silicon filters:

1. Ease of control of the moisture which affects the coating quality.
2. Ease of vapor access to any irregular channels where the access of liquid would be limited by capillary forces.
3. No toxic solvent is used in vapor phase deposition and contamination is minimized.
4. Incorporation in the standard filter testing protocol, which requires a nitrogen pass-through test. The

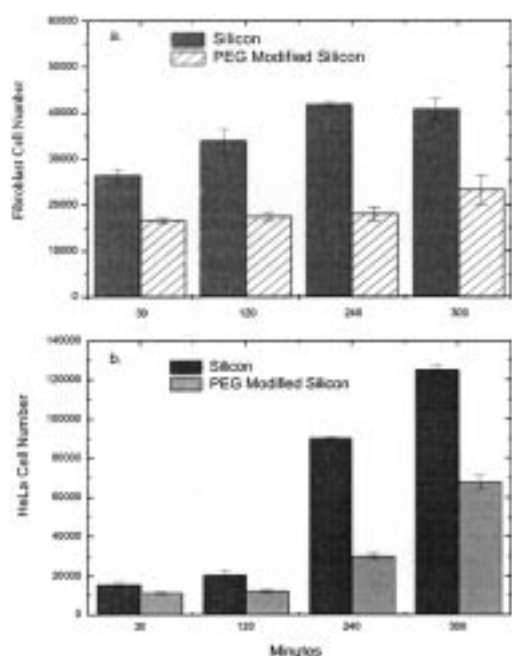


Fig. 27. Adhesion of fibroblast (a) and HeLa (b) cells onto silicon and PEG modified silicon surfaces.

chamber. The liquid at the exit of the chamber was collected and the mass was continuously recorded on a balance interfaced with a computer. The mass was converted to volume by the known density, and the flow rate was expressed in ml/min.

Results-vapor phase coating with VTS and GPTMS. VTS has a high vapor pressure at room temperature and the vapor phase coating was conducted at room temperature. After the vapor phase coating with VTS, the water contact angle of the wafer was $80\sim 90^\circ$. GPTMS has a lower vapor pressure and is less reactive than VTS. The temperature for GPTMS coating was chosen to be $90\sim 100^\circ\text{C}$. The water contact angle after GPTMS coating was around 60° . As seen in Figure 29 and Figure 30, the thickness of both coating was typically close to 1 nm.

In addition, the samples coated in vapor phase were characterized with Atomic Force Microscopy (AFM). The GPTMS coating shows a smooth surface with rms (root of mean squared) roughness of 0.12 nm, which is in the same roughness range of silicon wafers. AFM micrograph of VTS coating surfaces had rms roughness of 0.32 nm, with some wavy patterns, reflecting different texture of the surface. The coating composition was characterized with XPS. No residual chlorine was found by XPS on the VTS coating surface, indicating that chlorine was completely removed from the surface as HCl.

Solution coating with vinyltrichlorosilane (VTS). VTS is very reactive towards both silanol groups and water. Ideally in the absence of moisture, VTS would only react with the silanol groups on the surface of silicon wafers and filters to form a self assembled monolayer. In reality, it is difficult to control the moisture sufficiently effectively that only a monolayer forms. Figures 31 and 32 show that the coating thickness increased with both VTS concentration and reaction time.

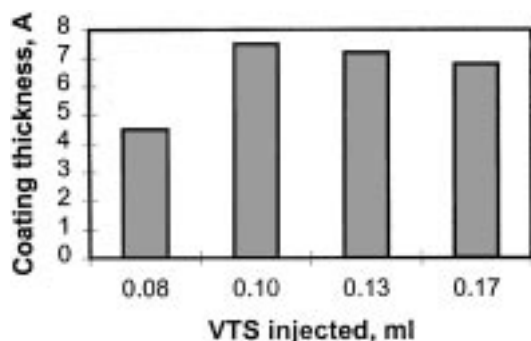


Fig. 29. VTS vapor phase coating at 23°C for 2 hours.

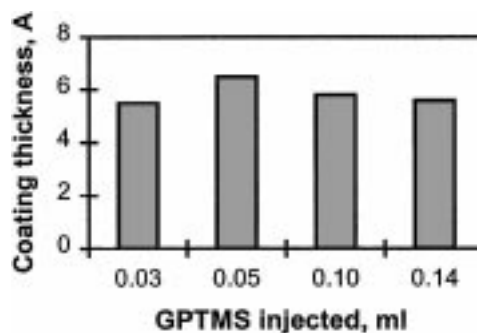


Fig. 30. GPTMS vapor phase coating at 100°C for 2 hours.

Figure 33 shows the proposed polymeric reactions in the formation of multilayers and aggregates in the presence of moisture. Both the physical dimensions of the coatings and their increasing thickness indicate that multilayers were formed under such conditions. Although it may be possible to obtain a “monolayer” by using very low concentrations and short contact time, it would be very difficult to control the quality of such a coating.

Water contact angles on wafer in the air after VTS coating were about 90° . The contact angles and coating thickness did not change after immersion in water or dilute H_2SO_4 for a week. A sample with a VTS coating 3.5 nm thick was heated in 1:1 mixture of 30% H_2O_2 and concentrated H_2SO_4 at 80°C for 10 minutes, and the contact angle dropped to almost zero but the coating thickness did not change appreciably (a few angstroms). This indicates that the coating was stable and the vinyl groups were oxidized to hydrophilic groups.

To test the polymerization hypothesis, silicon chips were coated with 5–10% mono-chlorotrimethylsilane in toluene. Since mono-chlorotrimethylsilane has only one chlorine per molecule, it is incapable of polymerization. Indeed the coating thickness was always less than 5 Å with water contact angle in air around 90° , which is

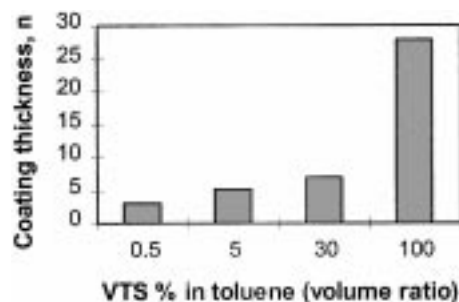


Fig. 31. VTS coating thickness increased with VTS concentration. Si wafers were immersed in VTS-toluene solution for 1 hour at 20°C .

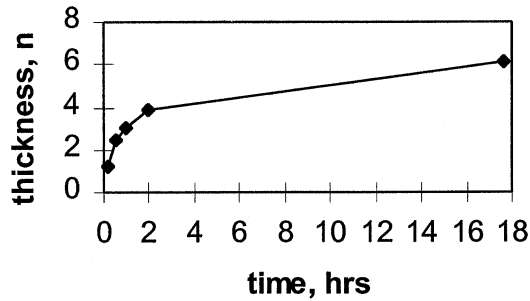


Fig. 32. VTS coating thickness increased with reaction time in 0.5% VTS-toluene at 20°C.

Table 3. Coating of silicon in monochlorovinyl dimethylsilane-toluene solution for 20 hours at 20°C

| % concentration (volume ratio) | coating thickness, Å | water contact angles, (in air) |
|--------------------------------|----------------------|--------------------------------|
| 0.5 | 1.2 ± 1.6 | 88° |
| 1.0 | 4.2 ± 1.7 | 86° |
| 2.0 | 4.4 ± 2.6 | 87° |
| 4.0 | 2.4 ± 1.4 | 86° |

indicative of a real monolayer. Similarly, the thickness of mono-chlorovinyl dimethylsilane coating was also below 5 Å, as shown in Table 3. This confirms the polymerization mechanism of VTS, leading to multilayers in the presence of traces of moisture. Coated samples were also examined with SEM.

Surface charge before and after the coating. To further probe the surface properties of the coating, silicon wafers were ground into a slurry with deionized water and then coated with VTS and GPTMS. The zeta potential of the fine particles in deionized water after each treatment is listed in Table 4. The zeta potential was greatly reduced by VTS vapor phase coating, but the surface was still negatively charged. The residual surface

Table 4. ζ potential of silicon particles in water before and after vapor phase coating

| Sample | Sample treatment | ζ potential, mV (average of 10 measurements) |
|--------|--|--|
| X | Silicon slurry (suspension) by grinding Si wafers in water, then dried at 90°C for 3 hours | -28.0 ± 3.5 |
| Y | Sample X was coated in VTS vapor at 23°C for 2 hours | -14.0 ± 2.4 |
| Z | Sample X was coated in GPTMS vapor at 97°C for 2 hours | 5.0 ± 2.0 |

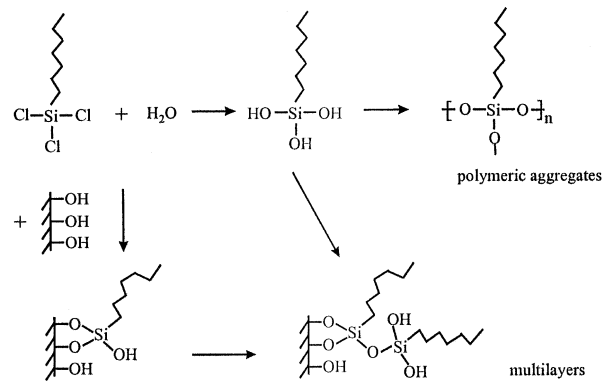


Fig. 33. Formation of polymeric aggregates or multilayers on silicon surface in solution coating when trace water is present in solution.

charge, in conjunction with the relative rough surface detected by AFM and coating thickness in Figure 33, suggests that the coating is more than an ideal monolayer and has residual silanol groups exposed to the air. In contrast, the surface after GPTMS vapor phase coating was almost neutral. This indicates that the surface is better covered by the longer chains in GPTMS than vinyl groups in VTS coating.

Coating of silicon filters and microfluidics. Silicon filters with channel sizes of microns were coated with alkylsilanes (GPTMS, VTS, and monochlorotrimethylsilane) in vapor phase, and tested with different fluids. Two filters were used and assigned codes F#1, F#2. Their dimensions are listed in Table 5.

In Table 6, the liquid flow rate through filter F#1 was compared before and after the coating. After the GPTMS coating and hydrolysis, the water contact angle was around 40°. No change in the flow rate of water was observed. Then, the filter was cooked in piranha for 2 hours, rinsed with water, and dried by passing nitrogen at room temperature, and then coated with VTS at room temperature. A smooth surface with bluish texture on the filter was seen after the VTS coating, and the water contact angle was around 90°. The bluish texture indicates the coating was not a real monolayer due to the residual trace water on the filter surface (the filter was not baked before coating), which is tolerable in 74 microns channels.

Table 5. Dimensions of silicon filters used in the coating and testing.

| | F#1 | F#2 |
|-----------------------------------|-----|-----|
| Channel length (L), cm | 2.2 | 2.2 |
| Channel width (w), μ m | 200 | 25 |
| Channel height (h), μ m | 74 | 1.8 |
| Number of channels per filter (n) | 27 | 20 |

Table 6. Coating of filter F#1 and comparison of flow rates (ml/min) at 3 PSI

| | Flow rate of water | Flow rate of 0.2 M NaCl | Flow rate of ethanol |
|--|--------------------|-------------------------|----------------------|
| Before any coating (filter cleaned in hot piranha, then rinsed and immersed in water before testing) | 6.23 ± 0.23 | 6.20 ± 0.29 | |
| After GPTMS coating at 70°C for 4 hours, then hydrolysis in 0.2 M H ₂ SO ₄ at 25°C overnight | 6.22 ± 0.14 | | |
| After cooking in piranha, filter was cleaned, dried, and coated with VTS at 23°C for 3 hours | 6.42 ± 0.23 | 6.44 ± 0.52 | 5.70 ± 0.21 |

After the VTS coating, the flow rate of water, 0.2 M NaCl, and ethanol was measured. It is seen in Table 6 that there was no difference between water and 0.2 M NaCl, indicating that electrostatic forces did not play a significant role in 74 microns channels. This observation agrees with the literature (6). In the classical fluid mechanics, the volume flow rate is inversely proportional to the fluid's viscosity for a fully developed flow between two parallel plates (Hele-Shaw geometry) or in a cylindrical conduct (Hagen-Poiseuille equation). It is interesting that the ratio of flow rate of water to that of ethanol was 1.13, very close to the viscosity ratio of ethanol (1.2 centipoise) to water (1.0 centipoise) at 20°C. This suggests that in 74 microns channels the flow obeys the classical fluid mechanics. In addition, changing the surface conditions (surface charge and hydrophilicity) in 74 microns channels had negligible effect on the liquid flow rate.

To compare the fluid flow in smaller filters (F#2) with large filters (F#1), water and ethanol were tested through filter F#2, as is shown in Table 7. First the filter F#2 was cooked in piranha for 3 hours at 120°C to remove any organic contaminants on filter surface, then rinsed with copious water, and immersed in water over night. The filter was loaded to the test chamber while the filter was still wet with water, followed by the flow test of water and ethanol, respectively. Table 7 shows that in 1.8 microns channels the flow rate of ethanol was much higher than that of water and the flow rate ratio was reversed when the channel size shrank from 74 microns to 1.8 microns.

After the fluid test, the filter F#2 was then dried and

coated with monochloro-trimethylsilane, which ensures a monolayer coverage and reduced surface charge. The filter was tested first with ethanol because ethanol is easy to permeate into the filter. After the data collection with ethanol, water was loaded to the chamber before ethanol completely drained (this avoids air-water interface inside filter channels). The flow rate of ethanol after the coating, being slightly decreased, was still greater than that of water. The reduced water flow rate in the second batch of test might be resulted from partial clogging by contaminants in water, but the trend of higher flow rate of ethanol than water was repeatable. This higher flow rate of ethanol than that of water was also reported by Kittilsland et al. in nominally submicron silicon filters. This may be due to the large difference in the surface tension between water and ethanol and the interaction of liquids with the channel surface.

4.3. Electroviscous effects in microchannels

The preliminary results reported in the previous section induced further investigations of the fundamentals of microfluidic mass transfer in our group. The problem, to be sure, is of outstanding significance in a much wider context: The importance of understanding capillary flow behavior is increasing every day, along with exponential growth in the number of applications that use fluid flow in microchannels. Food processing, separation methods and catalyst technology use fluid flow in closed channels of micron and sub-micron size phenomenon (hereinafter referred to as "microfluidics"). Biotechnology offers such popular applications for microfluidics systems as

Table 7. Coating of micromachined silicon filters and comparison of flow rate ratios of ethanol over water at 3 PSI.

| Filters | Treatment | Flow rate ratio of ethanol over water |
|------------------------------|--|---------------------------------------|
| F#1 Channel height 74 μm | After coating with VTS at 23°C for 3 hours, tested with water and ethanol, respectively | 0.89 ± 0.04 |
| F#2 Channel height 1.8 μm | After cleaning in piranha at 120°C for 3 hours, and with water, filter was tested first with water and then with ethanol | 1.76 ± 0.26 |
| F#2 Channel height 1.8 μm | Filter was dried and coated with monochlorotrimethylsilane, tested first with ethanol and then with water | 4.27 ± 1.1 |

viral filtration and protein separation (CH 1, 1995; Furlong and Beebe, 1997; MacNair et al., 1997; Aranha-Creado and Fennington, 1997), DNA analysis (Chan et al., 1997; Akerman, 1997; Woolley et al., 1997; Tang et al., 1997; Bousse et al., 1997; Webster and Mastrangelo, 1997), drug delivery (Henry et al., 1998; Reynaerts et al., 1997; Evans et al., 1997; Chu and Ferrari, 1995), and fast chemical/biological analysis of specimen (Shoji et al., 1988; Harrison et al., 1993; Anderson et al., 1997; Man et al., 1997). However, the rapid growth of microfluidic applications was not accompanied by a comparable growth in the theoretical analysis of fluid flow in closed microchannels. Our understanding of the theory of microfluidics is incomplete, and a satisfactory model is still lacking (Gravesen et al., 1993). There is currently no accord among scientists and engineers in the field of microfluidics on how equations of motion governing fluid flow in micron and sub-micron channels are different from equations of classical hydrodynamics. The general lack of understanding of the nature of microfluidics leads also to the import of ill-defined phenomenological parameters such as the friction coefficient or Darcy friction factor.

A theoretical analysis of the flow of polar liquids in microchannels of different geometrical cross-sections was performed by Burgreen and Nakache (1964), Rice and Whitehead (1965), and by Mala et al. (1997). When polar liquid is placed in contact with another phase (like the wall of the surrounding channel), a potential difference develops at the interface. Molecules of the polar liquid (dipoles) will re-orient themselves near the phase boundary. Ions or excess electrons present will cause a charge re-distribution at the interface, causing formation of the so-called electrical double layer (EDL). As pressure is applied to the liquid, charges inside the EDL start accumulating downstream while charges on the solid channel wall are immobile. That charge excess creates a potential drop that causes current flow

upstream. The flow of ions upstream creates a counter-flow that effectively reduces the liquid flux. It can also be presented analytically as either an increase in the friction coefficient or an increase in effective viscosity. The physical basis for the electrokinetic theory can be outlined in a series of sketches presented in Figure 34.

There have been very few experimental studies on liquid flow in microchannels. Pfahler et al. (1990) studied fluid flow in microchannels and observed that polar fluids (isopropanol) flow slower than predicted by the classical hydrodynamic theory while there is no corresponding retardation for non-polar fluids (silicon oil). One of the recent experimental works by Brody and his colleagues (1996) focused on the study of water flow in a microfabricated channel 11µm deep by 72µm wide. 0.9µm diameter fluorescent beads were passed along with the liquid to measure flow rate. A camera with an electronic shutter was used to make the successive images of the beads within short intervals of time. Beads velocities were then calculated. The authors argued that the results obtained demonstrate compliance with classical hydrodynamic theory. The graph of the beads velocities that was presented in the article showed a wide distribution of the velocities, where many beads had velocities well below the values predicted by classical hydrodynamic theory. The authors argued that those beads must have been close to the channel bottom (or top). That uncertainty in the bead position highlights one of the major weaknesses in that study: it was impossible to know the vertical position of the bead from the images. It is unknown if the beads were distributed uniformly along the depth of the channel or if they preferred to stay in the center of the channel. Without that information the interpretation of the average bead velocity is very difficult. Additionally, presence of the beads that carry surface charges is affecting the flow rate of polar liquids via electrokinetic effects.

The current work avoids using beads for flow

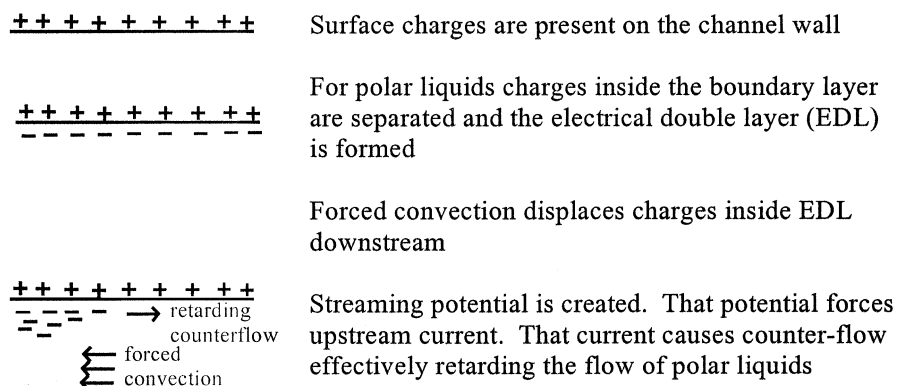


Fig. 34. Schematics of the electrokinetic effect in microfluidics.

visualization in microchannels. The mass flow rate is measured directly instead. Multiple identical channel array is used to increase the volume of the fluid passing through microchannels and, thus, to facilitate measurement of the mass flow rate by conventional means.

Experimental procedures. Four inch diameter silicon wafers polished on both sides were used as a substrate for creation of an array of microchannels. General wafer assembly is presented in Figure 35. The top wafer contains four rectangular entrances through windows 22 mm by 5 mm. The bottom wafer contains channels and the four exit windows of the same dimensions as the ones on the top wafer. All microfabrication was done under the room 100 conditions. Channels were produced first by depositing low-temperature oxide 2 micron thick (oxide thickness measurements are done by the Nanospec film thickness monitor) and then spinning 1.2 micron positive photoresist on the wafer B. The wafer was exposed to the UV light under the designed chrome mask in a contact printer. After the photoresist on the wafer B was developed, wafer was baked for 40 min at 120°C. Plasma etch was used to remove the oxide layer in the exposed areas (i.e., long wires defining channels). The remaining photoresist was removed and the wafer B was placed in an anisotropic EDP etch (320 g of pyrocatechol, 6 g of pyrazine, 320 ml of DI water and 1000 ml of ethylenediamine). Depth of the channels was controlled by the etch time. The channels' profile was obtained with a step profilometer. Resulting channels have the trapezoidal cross-section.

The remaining oxide was removed from the wafer B in HF solution. Wafers A and B underwent low temperature oxide deposition for 2 µm oxide thickness. By the lithography process outlined above, entrance and exit windows on wafers A and B correspondingly were defined and then etched (though the whole thickness of the wafer) in the EDP bath. The final oxide strip was

done in the concentrated HF acid. Channel profiles were measured. Wafers were put for 10 minutes at 80°C in the RCA solution of 5 H₂O : 1 NH₃OH : 1 H₂O₂ to clean the wafers of any organic traces. Wafers were washed in the water and spin-dried.

Wafers A and B were visually aligned and put on top of each other, after which the wafers were lightly pressed together in the center of the wafer assembly manually. The contact wave spread from the center to the outer edge of the wafers. At this point bonding was strong enough to hold wafers together and they could only be separated with the razor blade. Wafer assembly was held for 4 hours at 1000°C in a furnace. It was impossible to manually separate the wafers after the anneal. No distinguishable interface between the top and bottom parts of the assembly was observed when the unit was intentionally broken, signifying that chemical bonding took place. The unit could withstand pressures of at least 30 psi (it was not tested under higher pressure). The wafer assembly was sliced on the disk saw into the quarters producing four test units. Quality of bonding was verified by observing the test unit under the IR light of the contact printer. If there were some disbonded regions, diffraction fringes would be visible for disbonded regions several microns in size or larger. Test units with internal defects were discarded.

In the tests performed several test liquids including de-ionized (DI) particle-free water and ethyl alcohol, octane, NaCl solutions and n-propyl alcohol were forced under a constant pressure gradient through the channels of the test units. Before each experiment test liquids were filtered through 0.2 µm syringe polymer filter. Test unit was glued with the silicone adhesive to the wafer holder that fits within the test column. After a blank quarter wafer (i.e., without apertures) was glued to another holder and secured within the column, gas pressure was applied and the setup was checked for leaks. Liquid was rested on top of the test unit in the stainless steel column.

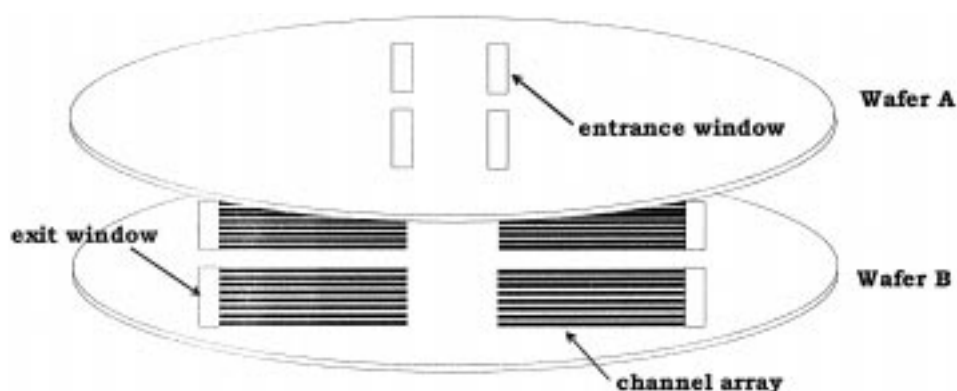


Fig. 35. Test unit assembly.

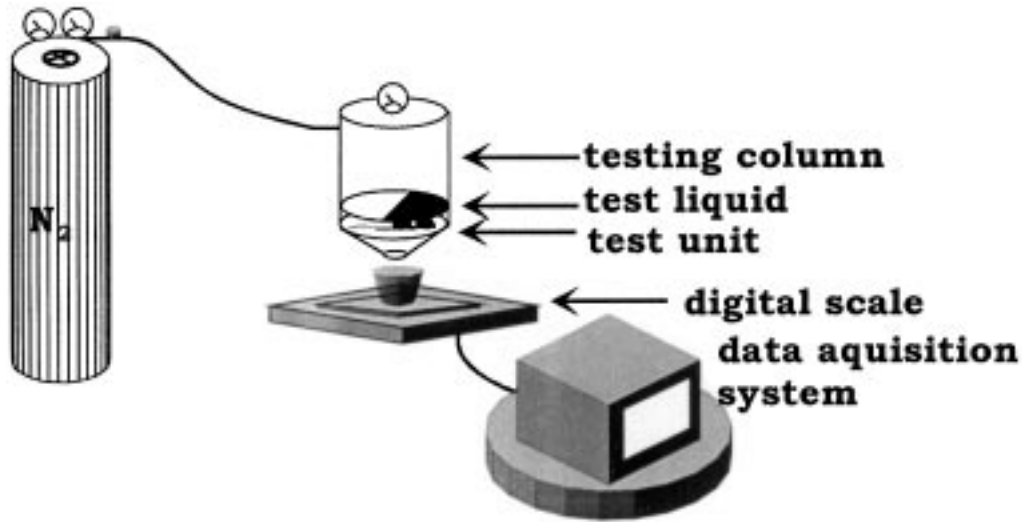


Fig. 36. Experimental set-up.

Mass flow rate was obtained as a weight of the liquid collected after it passed through the test unit. The weight was measured on the digital balance with equal time intervals of 2 seconds.

A schematic diagram of the experimental setup consisting of the nitrogen gas reservoir, stainless steel column, test liquid, test unit, digital scale and computer with the Strawberry data acquisition software, is presented in Figure 36. Zeta potential determination were made by Y. Wang and co-workers for slurry of silicon particles in DI water (-28 mV) (Wang, 1998).

The dimensions of the test units are listed in Table 8.

Results. Nearly fifty separate experiments were performed with various test units on several polar liquids (including de-ionized water, ethyl and propyl alcohol) and non-polar octane. Figure 37 presents typical result observed for polar liquids in microchannels of hydraulic diameters from 90 to 100 microns.

Classical hydrodynamic theory predicts the mass flow rate according to equation (1):

$$Q_m = \rho A n \frac{(D_h)^2 \Delta P}{2f(Re)\mu L}, \quad (1)$$

where ρ is the density of the liquid, A is the cross-sectional area of the channel, n is the number of channels in the array, ΔP is the pressure difference, D_h is the hydraulic diameter of the channel ($4 \times \text{area/perimeter}$), μ is the viscosity of the liquid, L is the length of the channel, $f(Re)$ is the parameter that depends on channel geometry. $f(Re)$ for trapezoidal channels was calculated numerically by Shah (1975).

As can be seen from Figure 37, there was generally retardation of the fluid flow for polar liquids as compared with the predictions of classical hydrodynamic theory. The average retardation for the DI water and alcohol was around 6%, while there was no retardation for a non-polar octane in the microchannels of 90 to 100 microns in

Table 8. Number of channels, geometric channel dimensions and hydraulic diameter ($4 \times \text{area/perimeter}$) for all test units

| Unit name | Number of channels | Channel width, μm | Channel height, μm | Channel length, mm | Cross-sectional area, m^2 | Hydraulic diameter, m |
|-----------|--------------------|------------------------------|-------------------------------|--------------------|------------------------------------|-----------------------|
| A | 27 | 200 | 74.5 | 20.5 | 1.098E-8 | 9.202E-5 |
| B | 27 | 206 | 73.5 | 21.5 | 1.132E-8 | 9.278E-5 |
| C | 25 | 216 | 77.1 | 21.5 | 1.245E-8 | 9.731E-5 |
| D | 27 | 200 | 74.0 | 21.5 | 1.093E-8 | 9.172E-5 |
| E | 27 | 200z | 74.0 | 19.5 | 1.093E-8 | 9.172E-5 |
| F | 27 | 216 | 83.2 | 21.0 | 1.306E-8 | 1.008E-4 |
| G | 27 | 201 | 72.2 | 20.5 | 1.081E-8 | 9.071E-5 |
| H | 27 | 200 | 74.0 | 21.5 | 1.093E-8 | 9.172E-5 |
| I | 20 | 200 | 1.8 | 20.0 | 3.577E-10 | 3.561E-6 |
| J | 20 | 200 | 2.2 | 21.5 | 4.366E-10 | 4.341E-6 |
| K | 20 | 200 | 2.0 | 20.5 | 3.972E-10 | 3.951E-6 |

hydraulic diameter. In microchannels with the hydraulic diameter from 3 to 4 microns the retardation of the DI water and ethyl alcohol was very significant at about 70 percent.

Comparison of the experimental data with the electrokinetic model predictions. First, derivation of the electrokinetic model will be outlined and the result for the expected mass flow rate will be given. More detailed derivation of the governing equations is given elsewhere (Kulinsky, 1998). The surface bears a uniform electrostatic potential, which decreases as one proceeds out into the fluid. Far away from the wall, the concentrations of positive and negative ions are equal. The electrostatic potential ψ , at any point near the surface is related to the net number of electrical charges per unit volume ρ in the vicinity of the point by the Poisson's equation (2). At the channel wall ψ is roughly equal to the zeta-potential ξ ,

$$\frac{d^2\psi}{dX^2} = -\frac{\rho}{\epsilon_0\epsilon}, \quad (2)$$

where X is the distance from the wall and the net charge density in a unit volume of fluid is given by:

$$\rho = (n^+ + n^-)ze = -2n_0ze \sinh(ze\psi/k_bT). \quad (3)$$

In the equation (3) above, n^+ and n^- are the number of ions of opposite charge z^+ and z^- in unit volume of the liquid, n_0 is the density of charge carriers for the electrolyte, e is the charge of an electron, k_b is the Boltzmann's constant and T is an ambient temperature.

When the pressure gradient forces liquid in the capillary to move, a charge accumulated downstream causes *streaming potential* E_s . That potential will cause an additional body force on the liquid, and Navier-Stokes equation will be modified to:

$$\mu \frac{d^2V_z}{dX^2} - \frac{dp}{dZ} + E_z\rho(x) = 0, \quad (4)$$

where E_z is the gradient of streaming potential E_s , μ is the viscosity of the liquid (assumed constant), and (dp/dZ) is the pressure gradient.

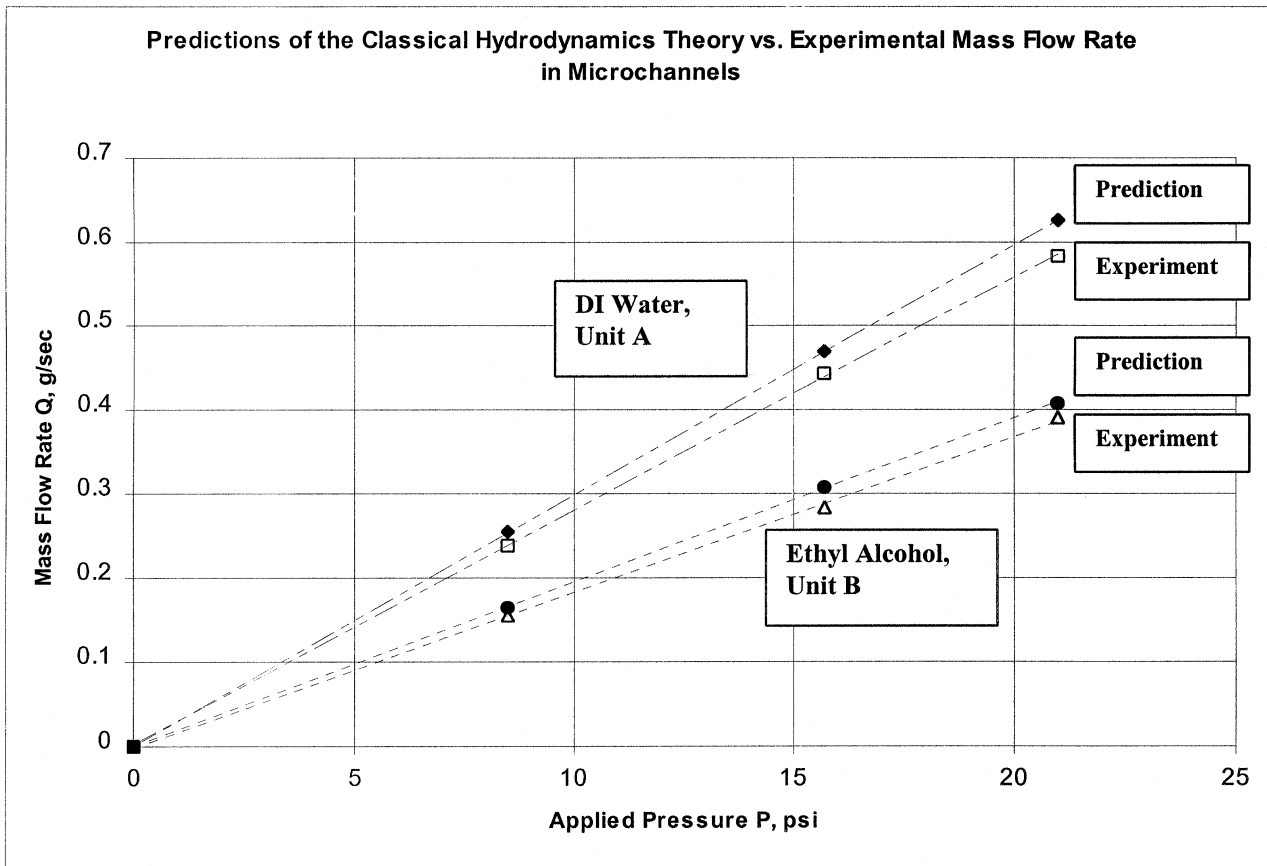


Fig. 37. Comparison of the experimentally observed mass flow rate in microchannels versus the theoretical predictions by the conventional hydrodynamic theory. De-ionized water flow in test unit A and ethyl alcohol flow in test unit B are considered.

In order to solve that equation of motion, equations (2) and (3) are used along with the fact that at steady state the net current through the liquid is zero. Non-slip at the channel wall is also used. In order to find closed-form solution, model was simplified to the flow between parallel plates of width w , height $2a$ and length l .

The resulting mass flow rate Q predicted by the electrokinetic theory is equal to:

$$Q(\xi) = \frac{2\rho w a^3 \Delta P}{\mu l} \left\{ \frac{1}{3} - \frac{\frac{1}{k} - \frac{2 \sinh(k)}{k^2} + \frac{2(\cosh(k)-1)}{k^3}}{\frac{\mu \lambda_0 \sinh(k)}{z e \xi n_0 \epsilon \epsilon_0} + \frac{2 z e \xi}{k_b T} \left(\frac{\cosh(k)-2}{2k} + \frac{1}{2 \sinh(k)} \right)} \right. \\ \left. \times \left[\frac{\cosh(k)-1}{k \sinh(k)} - 1 \right] \right\} \quad (5)$$

In equation (5) λ_0 is the electrical conductivity of the liquid, ρ is density of the liquid, ϵ_0 and ϵ are the dielectric permittivity of vacuum and of the liquid, respectively.

Dimensionless term k above is equal to:

$$k = \sqrt{\frac{2 n_0 z^2 e^2 a^2}{\epsilon \epsilon_0 k_b T}}. \quad (6)$$

The first term of the equation (5) is equivalent to the classical hydrodynamic predictions. However, the second negative term that depends on the zeta potential reduces the resulting mass flow rate and the retardation of the polar liquids is observed.

There was a general agreement between the predictions calculated on the base of the electrokinetic model and the observed retardation trends for polar liquids in microchannels. The predicted values for the mass flow rate of DI water and alcohol in microchannels of hydraulic diameter of 90 to 100 microns were somewhere between 2 to 12% lower than given by the equation (1) (range of the predicted values is a consequence of the finite resolution and uncertainties of the experiments). Those predictions are consistent with the experimental data that suggest retardation of the polar liquids to be on the order of several percent in the discussed microchannels. In agreement with the equation (6), the mass flow rate was directly proportional to the applied pressure (see Figure 4). The observed absence of retardation for non-polar octane, where charge separation is non-existent, is also consistent with the presented model.

In the microchannels with hydraulic diameter of 3 to 4 microns the electrokinetic predictions gave slightly overestimated retardation of 79% compared with 67 to 69% retardation observed. The possible reason for overestimation might be the overlap of the EDLs in very small microchannels that would tend to partly compensate charges and, subsequently, reduce retardation. Fluid flow data collected experimentally are consistent with the theoretical predictions of the electrokinetic model. A

conclusion can be drawn that electroviscous effects play a major role when the hydraulic diameter of microchannels is on the order of microns.

Effective viscosity. For Newtonian fluids the flow rate is inversely proportional to the physical viscosity of the fluid. Without regarding underlying physics of electroviscous phenomena, the decrease in the fluid flow in microchannels can be viewed as an increase in the so-called ‘‘effective viscosity’’. In the absence of any EDL effects, the flow rate in parallel-plate microchannel can be expressed as:

$$Q_m = \frac{2a^3 \Delta P w}{3l\mu} \rho. \quad (7)$$

We can re-write equation (5) in the same format as equation (7) using $\mu_{\text{eff}}(\xi)$ instead of μ . That ‘‘effective viscosity’’ will be:

$$\mu_{\text{eff}}(\xi) = \left\{ 1 - \frac{\frac{3}{k} - \frac{6 \sinh(k)}{k^2} + \frac{6(\cosh(k)-1)}{k^3}}{\frac{\mu \lambda_0 \sinh(k)}{z e \xi n_0 \epsilon \epsilon_0} + \frac{2 z e \xi}{k_b T} \left(\frac{\cosh(k)-2}{2k} + \frac{1}{2 \sinh(k)} \right)} \right. \\ \left. \times \left[\frac{\cosh(k)-1}{k \sinh(k)} - 1 \right] \right\}^{-1} \mu \quad (8)$$

The ratio M is now introduced to denote the increase in ‘‘effective viscosity’’ as related to real viscosity (a true physical property).

$$M(\xi) = \frac{\mu_{\text{eff}}(\xi)}{\mu}. \quad (9)$$

For channels of small hydraulic diameter the observed viscosity increase is very dramatic, as can be seen in Figure 38.

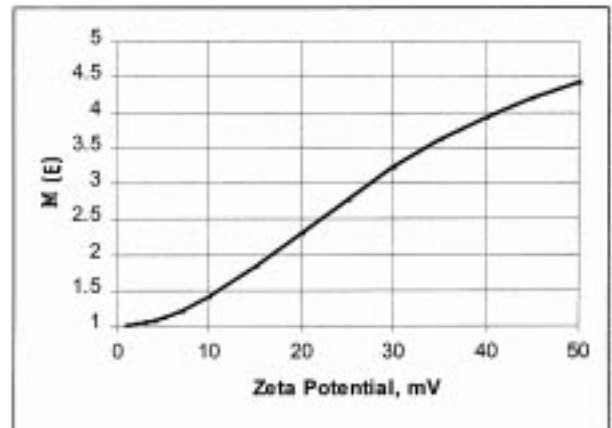


Fig. 38. Graph of the ratio M of the effective viscosity to physical viscosity (as a function of zeta-potential) for microchannels of the hydraulic diameter of 5 micron.

Friction constant in microfluidics. One of the most confusing issues in microfluidics is the usage of the so-called *friction factor*. It has been used excessively in many recent studies of fluid flow in microcapillaries. Unfortunately, as will be shown, the Darcy friction factor does not have a physical meaning in the microfluidics of polar liquids. The friction factor needs to be modified. The Darcy friction factor f for the given flow is:

$$f = \frac{8\tau_w}{\rho(V_{av})^2}, \quad (10)$$

where V_{av} is an average velocity in the channel. The *shear stress* at the wall τ_w for Newtonian fluids is directly related to the inclination of the velocity profile at the wall, as can be seen from equation (11):

$$\tau_w = \left| \mu \frac{dV_z}{dx} \right|_{x=a}. \quad (11)$$

The characteristic velocity profile in a small micro-channel, which was calculated using the electrokinetic governing equations, is presented in Figure 39.

The characteristic bow-like velocity profiles seen in Figure 39 are manifestations of the counter-flow, which is produced as a result of the streaming potential. At certain value of the zeta potential, velocity profile would be perpendicular to the channel wall. That would suggest that the shear stress and, therefore, the friction factor, should be zero. Mathematically, superfluidity is

implied. That, of course, is a fallacy. While the drag at the wall might be very small, it is more than compensated by the electroviscous drag.

The friction factor should be modified to reflect the effect of the retarding electrokinetic forces on the liquid. The proposed modified ‘‘effective friction factor’’ is:

$$f_{\text{eff}}(\xi) = \frac{h_f(\xi)8ag}{V_{av}(\xi)^2}, \quad (12)$$

where $h_f(\xi)$ is the total hydraulic head loss that includes both, the frictional drag head loss, as well as electroviscous head loss:

$$h_f(\xi) = -\frac{\tau_w(\xi)l}{\rho g a} + \frac{2n_0e^2z\xi^2 \cosh(k) - 1}{k_bT\rho g \sinh(k)k} E_s(\xi). \quad (13)$$

If zeta-potential is equal to zero, then total head loss has only a drag head loss term and the effective friction factor can be simplified to $f = 8\tau_w/(\rho V_{av})$, which is the well-known Darcy friction factor. For non-zero zeta-potential the effective friction factor can be substantially larger than the Darcy friction factor, as can be seen from the graph in Figure 40, where the ratio θ of the effective friction factor to the Darcy friction factor is presented.

$$\theta(\xi) = \frac{f_{\text{eff}}(\xi)}{f}. \quad (14)$$

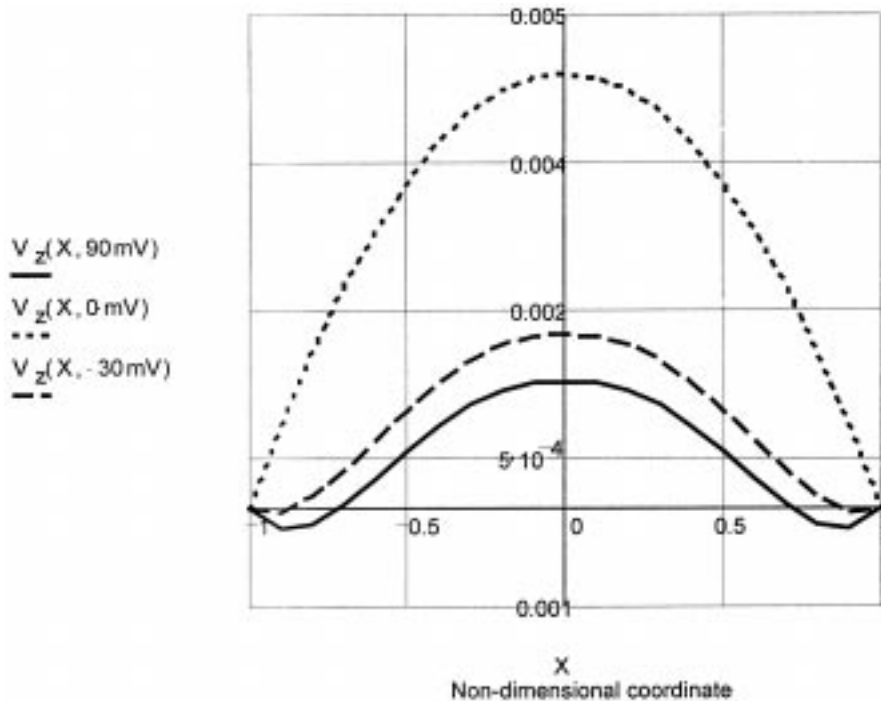


Fig. 39. Characteristic velocity profiles for various zeta potentials in the microchannel of the hydraulic diameter of 5 micron.

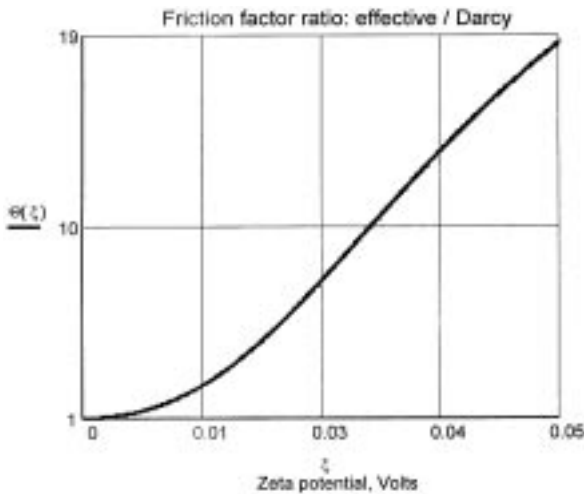


Fig. 40. Graph of the ratio θ of the effective friction factor f_{eff} to the Darcy friction factor in the microchannel of the hydraulic diameter of 5 micron.

As we can see, the electroviscous effect makes a big impact on the effective friction factor. Even at small values of the zeta-potential, the effective friction factor is several times larger than the Darcy friction factor.

Summary. The electrokinetic effects dominate the flow of polar liquids in the closed channels of micron and sub-micron size. The governing laws of the fluid flow in microchannels were analyzed. A series of experiments performed on the polar fluid flow in microchannels corresponds well with the presented electrokinetic theory. In order to increase the flow through microchannels, the retarding streaming potential should be minimized. That can be accomplished by reducing the zeta potential. The zeta potential might be reduced by either modifying the surface of the channel wall (Wang, 1998; Shah, 1975; Kulinsky, 1998), or by adding certain ions to the polar liquid (Kulinsky, 1998). Non-polar liquids experience no electrokinetic retardation. Based on the electrokinetic analysis it is expected to observe the increase in the effective viscosity for polar liquids in microchannels. The Darcy friction factor can not be applied to the field of microfluidics and should be modified. The *effective friction factor* that is applicable to the conventional hydrodynamics as well as to microfluidics is suggested.

4.4. Immunografts on microfabricated surfaces

Increasingly, BioMEMS devices are utilizing both microfabrication and biochemistry to create more complex devices. For example, surfaces can be patterned with functional groups, making it possible to attach cellular structures such as microtubules or cells in specific locations and in specific shapes (Turner et al.,

1995; Lom et al., 1993). As BioMEMS devices develop, it will be desirable to control chemical properties at the length-scale of the geometric features on the device. In general, organosilanes are the molecules of choice for the modification of inorganic surfaces found in microfabricated devices, since they can be used to couple organic functional groups to practically any oxide surface. The substituted organic groups can be used to alter surface properties, as for example, converting a hydrophilic oxide into a hydrophobic surface (Brzoska et al., 1994). They can also be used to link macromolecules to a surface, such as in the immobilization of proteins to silica supports (Bhatia et al., 1989; Flounders et al., 1995).

As the ability to conduct chemical modifications on spatially confined regions improves, analytical methods are needed that can assess the chemical properties on exceedingly small surfaces. To address this need, a quantitative method was recently developed that utilizes confocal microscopy to estimate the number of functional groups added to microfabricated devices (Nashat et al., 1998). The method only requires a fluorescent-tagged molecule that binds specifically to the chemical group to be detected. With appropriate calibration, a quantitative estimate of the functional group surface density can be obtained at the resolution of the confocal microscope (equivalent to $0.035 \mu\text{m}^2$ utilizing a $60\times$ objective lens with a numerical aperture of 1.4). Thus, the optimal resolution of this measurement method matches quite well with the minimum dimensions that can currently be microfabricated (on the order of 100's of nanometers).

As a test of this method, simple rectangular-shaped particles were microfabricated from silicon dioxide with dimensions that would potentially allow for *in vivo* transit through mammalian vasculature (thickness of $0.9 \mu\text{m}$, and lengths and widths varying from 1 to $3 \mu\text{m}$). After microfabrication, the particles were released from silicon wafers and suspended in solution, after which they were chemically modified. Three chemical functionalities were added to the surface of the devices: an amine group via aminosilanization; a thiol group via mercaptosilanization; and an antigen binding site via covalent attachment of an antibody.

To probe for the presence of active amines, an amine-reactive fluorescent probe, fluorescein succinimidyl ester (FSE), was reacted with the surface of the devices, and after washing, the fluorescence signal from the surface of the device was measured. Microparticles that were chemically modified with non-reactive alkane groups (using octylsilane or propylsilane) and untreated microparticles were used to account for non-specific adsorption of the fluorescent probe. To detect chemically active thiol groups, the thiol-reactive probe fluorescein maleimide (FM) was used. The fluorescence signal from

solutions of different concentrations of FM or FSE and at different confocal laser powers were used to obtain calibration curves that gave a quantitative estimate of the fluorescence emission from a single fluor. Thus, the signal measured from the surface of the particles (whether due to specific or non-specific adsorption) could be converted into the number fluors on the surface. Since fluorescence intensity from a fluor is extremely sensitive to environmental conditions, calibration of the fluorescence emission from the probe must be performed during each experiment. To estimate the number of antigenic sites that could be grafted to the particle surface, fluorescein-labeled human IgG antibodies (FITC-huIgG) were covalently attached to thiol-coated particles using the heterobifunctional cross-linker, succinimidyl 4-(N-maleimidomethyl)-cyclohexane-1-carboxylate (SMCC). Again, non-reactive, propyl-coated particles were used as controls, and calibration was performed on solutions of the fluor-tagged antibody.

In these experiments, adsorption of fluorescent probes (FM or FITC-huIgG) was always greater to surfaces presenting a thiol functional group than to alkane-coated or bare oxide surfaces (13 times higher for FM, and 2 times higher for the antibody). In contrast, adsorption of an amine-reactive fluorescent probe (FSE) was significantly greater than non-specific adsorption to an alkane-coated microparticle only after they had been exposed to buffer for greater than one month; after 6 hours in buffer, alkane-coated surfaces bound as much FSE as amine-derivatized particles. Further, the concentration of fluorescein bound to thiols averaged 6.6 times higher than to amine-substituted surfaces. As is clear from these results, confocal laser microscopy allows quantitative comparison of different surface modifications. Furthermore, since the resolution of the method is $0.035 \mu\text{m}^2$, it is possible to evaluate the uniformity of the coating across the surface as small as $1 \times 1 \mu\text{m}$. Thus, the method can detect any heterogeneities, whether desired or accidental, in the surface modification steps.

Using the confocal microscope, the maximum surface density of FM bound to thiol groups was measured to be 6.3×10^{-3} fluors per nm^2 ; the maximum surface density of FSE bound to amines was 1.0×10^{-3} fluors per nm^2 . These measurements are at least two orders of magnitude lower than values of functional group surface density obtained with other techniques. In the case of immobilized antibody, however, the surface density of IgG measured by confocal microscopy (9.71×10^{-4} IgG/ nm^2) agrees reasonably well with other values reported in the literature and corresponds to 8.3% of an antibody monolayer (Williams and Blanch, 1994). Bhatia et al. (1989; Bhatia et al. 1993) immobilized between 2.6×10^{-3} and 3.8×10^{-3} IgG molecules per nm^2 on

thiol-coated glass coverslips, using the heterobifunctional crosslinker GMBS. Renken et al. (1996) obtained a surface density of 2.6×10^{-3} IgG per nm^2 on aminosilanized LiNbO_3 using glutaraldehyde.

Since the four-ringed fluorescein structure occupies approximately 1 nm^2 when lying flat on the surface, the measured values of FM or FSE surface adsorption correspond to less than 1% of a parallel monolayer of fluors, thus ruling out the possibility of surface saturation. It is hypothesized that the discrepancies between the confocal measurements and literature values arise from calibration errors. In particular, the local environment of the fluor when in solution (during calibration) may be greatly different than when attached to the surface. As an example, experiments with FITC labeled RNAase on latex spheres showed that as the surface density increases, a five fold decrease in quantum yield can result (Robeson and Tilton, 1995). Thus, the estimate of fluorescence yield obtained by solution calibration may over-estimate the yield from fluors attached to a surface and thus under-estimate the number of fluors bound to the surface. However, in the case of immobilized antibodies, the fluor is in approximately the same environment in both the calibration solution and when immobilized to the microparticle: namely, attached to the "surface" of the protein, and thus less subject to changes in quantum yield. Thus, laser confocal microscopy appears to be successful at measuring the local surface density of immobilized macromolecules, provided appropriate calibrations are made. Furthermore, this method has the ability to measure chemical reactivity on a length-scale consistent with the limits of microfabrication technology.

Concluding Remarks

In four years of research at the Biomedical Microdevices Center at UC Berkeley, we have introduced and demonstrated innovative fabrication protocols that permit the manufacturing of silicon-based nanoporous membranes of extreme uniformity. The nanomembranes were proven effective in modulating immunorecognition, and shielding xenografts from acute adverse rejection phenomena. Their ability to release immunomolecules at controlled rates was established. These results strongly support the proposed use of microfabricated biocapsules for immunoisolated cell xenografts, and the passive release of therapeutic biomolecules. Surface modification protocols were presented and fully characterized, that afford the engineering of protein resistant and hemocompatible micromachined surfaces by physisorption and the silane-mediated grafting of PEO/PEG. The covalent attachment

of immunoglobulins to silica test surfaces and micro-machined particles was demonstrated, and verified quantitatively by confocal microscopy. Micromachined, surface modified channels were employed to investigate the dynamics of microfluidic flow in channels in the presence of electroviscous drag phenomena.

Acknowledgments

Financial support for the development of nanomembrane and biocapsule micromachining, biocompatibility, and characterization protocols (TD, MF, DH, LK, JT, YW, MZ) was provided by MicroFab BioSystems, a wholly-owned subsidiary of Vion Pharmaceuticals. The study of antibody grafting and their quantitative detection by confocal microscopy (MF, AN) was supported by the National Science Foundation, through MF's National Young Investigator Award. The authors gratefully acknowledge the support of others that have participated in the projects of UC Berkeley's Biomedical Microdevices Center, and have directly influenced the research presented herein: Ruby Chen, Wen-Hua Chu, Tony Huen, Mario Moronne, and Robert Szema.

References

- B. Akerman, *Journal of Chemical Physics* **106**, 6152–9, (1997).
- T. Akin and K. Najafi K, *IEEE Transactions on Biomedical Engineering* **41(4)**, 305–313 (1994).
- Y.B. Aldenhoff, *J. Biomed. Mater.* **29**, 17–928, (1995).
- J.J. Altman, *Pancreatic Islet Cell Transplantation*, C. Ricordi, ed. 216–222, (1991).
- R.C. Anderson, *Tech. Digest IEEE Transducers*, 477–80, (1997).
- H. Aranha-Creado and G.J. Fennington Jr., *J. Pharm. Sci. Tech.* **51**, 208–12, (1997).
- G.T. Baxter, L.J. Bousse, T.D. Dawes, J.M. Libby, D.N. Modlin, J.C. Owick, and J.W. Parce, *Clinical Chemistry* **40(9)**, 1800–1804 (1994).
- G. Beaman and D. Briggs, *High resolution XPS of organic polymers*. John Wiley & Son (1992).
- D. Beyer, T.M. Bohanon, W. Knoll, and H. Ringsdorf, *Langmuir* **12**, 2514–2518, (1996).
- S.K. Bhatia, L.C. Shriver-Lake, K.J. Prior, J.H. Georger, J.M. Calvert, R. Bredehorst, and F.S. Ligler, *Analytical Biochemistry* **178**, 408–413, (1989).
- S.K. Bhatia, J.L. Teixeira, M. Anderson, L.C. Shriver-Lake, J.M. Calvert, J.H. Georger, J.J. Hickman, C.S. Dulcey, P.E. Schoen, and F.S. Ligler, *Analytical Biochemistry* **208**, 197–205, (1993).
- L. Bousse, A. Kopf-Sill, and J.W. Parce, *Tech. Digest IEEE Transducers*, 499–502, (1997).
- M.D. Brendel, S.S. Kong, R. Alejandro, and D.H. Mintz, *Cell Transplantation* **3**, 427–35, (1994).
- J.P. Brody, T.D. Osborn, F.K. Forster, and P. Yager, *Biophysical Journal* **71**, 3430–41, (1996).
- C.R. Brundle, C.A. Evans, and S. Wilson, eds, *Encyclopedia of Materials Characterization*. Butterworth-Heinemann, Boston (1992).
- J.B. Brzoska, I.B. Azouz, and F. Rondelez, *Langmuir* **10**, 4367–4373, (1994).
- K. Burczak, T. Fujisato, M. Hatada, and Y. Ikada, *Biomaterials* **15**, 231–238, (1994).
- D. Burgreen and F.R. Nakache, *J. Phys. Chem.* **68**, 1084–91, (1964).
- R. Calafiore, G. Basta, A. Falorni, L. Avellini, and P. Brunetti, *Horm. Metab. Research* **25**, 209–214, (1990).
- L.T. Calhan, *Advanced Materials* **7(12)**, 1033–7, (1995).
- K.C. Chan, G.M. Muschik, and H.J. Issaq, *Journal of Chromatography* **695**, 113–5, (1997).
- W. Chu and M. Ferrari, *SPIE Proceedings* **2593**, (1995).
- Wen-Hua Chu and M. Ferrari, *Proc. SPIE*, 9–20, (1995).
- W. Chu, T. Huen, J. Tu, and M. Ferrari, *SPIE Proc. of Micro- and Nanofabricated Structures and Devices for Biomedical Environmental Applications*, Ed. P.L. Gourley, **2978**, 111–122, (1996).
- C.K. Colton, *Cell Transplantation* **4(4)**, 415–436, (1995).
- Colton and E. Avgoustiniatos. *Transactions of the ASME* **113**, 152–170 (1991).
- R.G. Craig, ed., *Restorative Dental Materials*, 9th Ed. Mosby-Year, Inc., (1993).
- T.A. Desai, D. Hansford, and M. Ferrari, *J. Membrane Science*. Accepted February 1999.
- T.A. Desai, J. Tu, G. Rasi, P. Borboni, and M. Ferrari, *Biomedical Microdevices* In print, (1998b).
- T.A. Desai, M. Ferrari, and G. Mazzoni, *Materials and Design Technology*, Ed. T. Kozik. ASME 1995, 97–103, (1995).
- T.A. Desai, W.H. Chu, J.K. Tu, G.M. Beattie, A. Hayek, and M. Ferrari, *Biotechnology and Bioengineering* **57**, 118–120, (1998).
- T.A. Desai, W.H. Chu, J. Tu, P. Shrewsbury, and M. Ferrari, *Micro- and Nanofabricated Electro-Optical Mechanical Systems for Biomedical and Environmental Applications*, P.L. Gourley, ed. BIOS.
- T.A. Desai, W.H. Chu, G. Rasi, P. Sinibaldi-Vallebona, P. Borboni, G. Beattie, A. Hayek, and M. Ferrari, *Micro and Nanofabricated Electro-Optical- Mechanical Systems for Biomedical and Environmental Application* **3258**, 40–47, (1998a).
- K.E. Dionne, B.M. Cain, R.H. Li, W.J. Bell, E.J. Doherty, D.H. Rein, M.J. Lysaght, and F.T. Gentile, *Biomaterials* **17**, 257–266, (1996).
- D.J. Edell, J.N. Churchill, and I.M. Gourley, *Biomat. Med Dev. Artif. Org.* **10(2)**, 103–122 (1982).
- C.S. Effenhauser, A. Manz, and H.M. Widmer, *Analytical Chemistry* **67**, 2284–2287 (1995).
- J. Evans, D. Liepmann, and A.P. Pisano, *Proc. IEEE MEMS* **97**, 96–101, (1997).
- M. Ferrari, W.H. Chu, T. Desai, D. Hansford, T. Huen, G. Mazzoni, and M. Zhang, *Thin Films and Surfaces for Bioactivity and Biomedical Application*, C.M. Cotell, A.E. Meyer, S.M. Gorbaklin, and G.L. Grobe (eds.), *MRS*, **414**, 101–106, (1996).
- M. Ferrari, W.H. Chu, T.A. Desai, and J. Tu, *Advanced Manufacturing Systems and Technology*. Ed. E. Kuljanic. CISM Courses and Lectures 372. Springer Verlag, 559–567, (1996).
- A.W. Flounders, D.L. Brandon, and A.H. Bates, *Applied Biochemistry and Biotechnology* **50**, 265–283, (1995).
- S.A. Fodor, *Science* **277**, 393–395 (1997).
- C.D. Furlong and D.J. Beebe, *Proc. IEEE Medicine and Biology* **248–9**, (1997).
- A. Gerasimidi-Vazeo, *Transplantation Proceedings* **24**, 667–668, (1992).
- M. Goosen, *Biotechnology Bioengineering* **27**, 146–150, (1985).
- P.L. Gourley, *Nature Medicine* **2(8)**, 942–944 (1996).
- P. Gravesen, J. Branebjerg, and O.S. Jensen, *J. Micromech. Microeng.* **3**, 168–82, (1993).
- D. Hansford, *Master's Thesis*, University of California, Berkeley, (1996).

- D. Hansford, T. Desai, J. Tu, and M. Ferrari, Micro and Nanofabricated Electro-Optical-Mechanical Systems for Biomedical and Environmental Application, **3258**, 164–168, (1998).
- D.J. Harrison, Tech. Digest IEEE Transducers, 403–6, (1993).
- D.J. Harrison, K. Fluri, K. Seiler, Z. Fran, C.S. Effenhauser, and A. Manz, Science **261**, 895–897 (1993).
- S. Henry, Proc. IEEE MEMS 98, 494–8, (1998).
- S.H. Ho, K.M. Gooding, and F.E. Regnier, J. Chromatography **120**, 321–333, (1976).
- G. Hsuie, S. Lee, and P.C. Chang, J. Biomater. Sci. Polymer Edn. **7**, 839, (1996).
- X.C. Huang, M.A. Quesada, and R.A. Mathies, Analytical Chemistry **64(8)**, 2149–54 (1992).
- U. Jonsson, G. Olofsson, M. Malmqvist, and I. Ronnberg, Thin Solid Films **124**, 117–123, (1985).
- K.R. Kamath, M.J. Danilich, R.E. Marchant, and K. Park, J. Biomater. Sci. Polymer Edn. **7(11)**, 977–988, (1996).
- G.T.A. Kovacs, C.W. Stormont, M. Halks-Miller, C.R. Belczynski, C.C. Della Santina, E.R. Lewis, and N.I. Maluf, IEEE Transact. Biomed. Eng. **41**, 567–577 (1994).
- L. Kulinsky, *Study of the Fluid Flow in Microfabricated Microchannels*, Ph. D. thesis, University of California, Berkeley, (1998).
- P. Lacy, O.D. Hegne, A. Gerasimidi-Vazeou, F.T. Gentile, and K.E. Dionne, Science **254**, 1728–1784, (1992).
- K.J. Lafferty, Diab. Nutr. Metab. **2**, 323–332, (1989).
- P. Langer and R. Schnabel, Chem. Biochem. Eng. Q **2(4)**, 242–244, (1988).
- R. Lanza and W. Chick, Scientific American Science & Medicine **2(4)**, 16–25, (1995).
- R.P. Lanza, S.J. Sullivan, and W.L. Chick, Diabetes **41**, 1503–1510, (1992).
- B. Lassen, Clinical Materials **11**, 99–103, (1992).
- F. Lim and A.M. Sun, Science **210**, 908–910 (1980).
- B. Lom, K.E. Healy, and P.E. Hockberger, Journal of Neuroscience Methods **50**, 385–397, (1993).
- R. Maboudian and R.T. Howe, J. Vacuum Science and Technology **B15(1)**, 1–20, (1997).
- J.E. MacNair, Rapid Communications in Mass Spectrometry **11**, 1279–85, (1997).
- G.M. Mala, Dongqing Li, and J.D. Dale, Int. J. Heat Mass Transfer **40**, 3079–88, (1997).
- P.F. Man, D.K. Jones, and C.H. Mastrangelo, Proc. IEEE MEMS 97, 311–6, (1997).
- H.N. McConnell, J.C. Owicki, J.W. Parce, D.W. Miller, G.T. Baxter, H.G. Wada, and S. Pitchford, Science **257(5078)**, 1906–1912 (1992).
- Microfabrication Technology for Research and Diagnostics*. Cambridge Healthtech Institute, MA (1995).
- M. Morpurgo, F.M. Veronese, D. Kachensky, and J.M. Harris, Bioconjugate Chem. **7**, 363–368, (1996).
- M. Mrksich and G.M. Whitesides, Ann. Rev. Biophys. Biomol. Struct. **55–78**, (1996).
- A.H. Nashat, M. Moronne, and M. Ferrari, Biotechnology and Bioengineering **60(2)**, 137–146, (1998).
- G.M. O'Shea, M.F.A. Goosen, and A.M. Sun, Biochim. Biophys. Acta **804**, 133–136, (1984).
- J. Pfahler, Sensors Actuators A **21–23**, 431–4, (1990).
- J. Piehler, A. Brecht, K.E. Geckeler, and G. Gauglitz, Biosensors and Bioelectronics **11**, 579–590, (1996).
- J. Renken, D. Reiner, and M. Grunze, Analytical Chemistry **68**, 176–182 (1996).
- D. Reynaerts, J. Peirs, and H. van Brussel, Sensors Actuators **A61**, 455–62, (1997).
- C.L. Rice and R. Whitehead, J. Phys. Chem. **69**, 4017–24, (1965).
- E. Richter, G. Fuhr, T. Muller, S. Shirley, S. Rogaschewski, K. Reminer, and C. Dell, Journal of Materials Science: Materials in Medicine **7**, 85–97, (1996).
- J.L. Robeson and R.D. Tilton, Biophysical J. **68**, 2145–2155, (1995).
- P.E. Ross, Scientific American 18–20, (1993).
- T.N. Salthouse and B.F. Matlaga, J. Biomater. Med. Dev. and Art. Orgs **3(1)**, 47–56, (1975).
- Santini, Cima and Langer, Nature **397**, 335–338 (1999).
- D.W. Scharp, N.S. Mason, and R.E. Sparks, World J. Surg. **8**, 221–229 (1984).
- R. Schnabel and P. Langer, J. Chromatography **544**, 137–146, (1991).
- G. Scott and M. Mowrey-Mckee, Current Eye Research **15(5)**, 461–466, (1996).
- R.K. Shah, Int. J. Heat Mass Transfer **18**, 849–62, (1975).
- S. Shoji, M. Esashi, and T. Matsuo, Sensors Actuators **14**, 101–7, (1988).
- C.M. Strasser, P.H. Dejardin, J.C. Galin, and A. Schmitt, M. J. Biomed. Mater. Res. **23**, 1385–1393, (1989).
- M.E. Sugamori, ASAIO Trans. **35**, 179–799, (1989).
- T. Tang, G. Ocvirk, and D.J. Harrison, Tech. Digest IEEE Transducers 523–6, (1997).
- J.A. Tesk, MRS Symp. Proc. **110**, 177–84, (1989).
- Y.C. Tseng and K. Park, J. Biomed. Mater. Res. **26**, 373–91, (1992).
- J.K. Tu, T. Huen, R. Szema, and M. Ferrari, *SPIE Proc. of Micro- and Nanofabricated Structures and Devices for Biomedical Environmental Applications*, Ed. P.L. Gourley, **3258**, 148–155, (1998).
- T.C. Turner, C. Chang, F. Fang, S.L. Brandow, and D.B. Murphy, Biophysical Journal **69**, 2782–2789, (1995).
- A. Ulman, Chemical Reviews **96**, 1533–1554, (1996).
- W.D. Volkmuth, T. Duke, R.H. Austin, and E.C. Cox, Proc. Natl. Acad. Sci. USA **92(15)**, 6887–6891 (1995).
- Y. Wang and M. Ferrari, *SPIE Proc. of Micro- and Nanofabricated Structures and Devices for Biomedical Environmental Applications*, Ed. P.L. Gourley, **3258**, 20–28, (1998).
- T. Wang, I. Lacik, M. Brissova, A. Anilkumar, A. Prokop, D. Hundeler, R. Green, K. Shahrokhi, and A. Powers, Nature Biotechnology **15**, 358–362, (1997).
- Y. Wang, *Surface Modification of Polymeric Membranes and Silicon Filters*, Ph. D. thesis, University of California, Berkeley, (1998).
- S.R. Wasserman, Y.T. Tao, and G.M. Whitesides, Langmuir **5**, 1074–1081, (1989).
- C.J. Weber, *Pancreatic Islet Cell Transplantation*, C. Ricordi, ed., 177–189, (1991).
- J.R. Webster and C.H. Mastrangelo, Tech. Digest IEEE Transducers, 503–6, (1997).
- R.A. Williams and H.W. Blanch, Biosensors and Bioelectronics **9**, 159–167, (1994).
- K.D. Wise, Annual Conference of the IEEE Engineering in Medicine and Biology Society **12(5)**, 2334–2335 (1990).
- A.T. Woolley and R.A. Mathies, Proc. Natl. Acad. Sci. USA **91**, 11348–11352 (1994).
- A.T. Woolley, G.F. Sensabaugh, and R.A. Mathies, Analytical Chemistry **69**, 2181–6, (1997).
- M. Zhang and M. Ferrari, Biotech. Bioeng. **56**, 618–625, (1997).
- M. Zhang and M. Ferrari, Biomedical Microdevices **1(1)**, 81–89 (1998b).
- M. Zhang and M. Ferrari, “Enhanced blood compatibility of silicon coated with a self-assembled poly(ethylene glycol) and monomethoxypoly(ethylene glycol)”. In: Gourley, P. editor. Micro and nanofabricated electro-optical-mechanical systems for biomedical and environmental application. 1998a. SPIE Proceeding Series. 15–19.
- Miqin Zhang, Tejal Desai, and Mauro Ferrari, Biomaterials, **19**, 953–960, (1998).